Fragment-orbital-dependent spin fluctuations in the single-component molecular conductor [Ni(dmdt)$_2$]

Taiki Kawamura ● and Akito Kobayashi ●
Department of Physics, Nagoya University, Nagoya, Aichi 464-8602, Japan

Motivated by recent nuclear magnetic resonance experiments, we calculated the spin susceptibility, Knight shift, and spin-lattice relaxation rate ($1/T_1T$) of the single-component molecular conductor [Ni(dmdt)$_2$] using the random phase approximation in a multi-orbital Hubbard model describing the Dirac nodal line electronic system in this compound. This Hubbard model is composed of three fragment orbitals and on-site repulsive interactions obtained using *ab initio* many-body perturbation theory calculations. We found fragment-orbital-dependent spin fluctuations with the momentum $\mathbf{q} = \mathbf{0}$ and an incommensurate value of the wave number $\mathbf{q} = \mathbf{Q}$ at which a diagonal element of the spin susceptibility is maximum. The $\mathbf{q} = \mathbf{0}$ and $\mathbf{Q}$ responses become dominant at low and high temperatures, respectively, with the Fermi-pocket energy scale as the boundary. We show that $1/T_1T$ decreases with decreasing temperature, but starts to increase at low temperature owing to the $\mathbf{q} = \mathbf{0}$ spin fluctuations, while the Knight shift keeps monotonically decreasing. These properties are due to the intramolecular antiferromagnetic fluctuations caused by the characteristic wave functions of this Dirac nodal line system, which is described by an n-band ($n \geqslant 3$) model. We show that the fragment orbitals play important roles in the magnetic properties of [Ni(dmdt)$_2$].

I. INTRODUCTION

Dirac electron systems in solids are of interest to many researchers because of not only their quantum transport phenomena [1–4] and large diamagnetism [5,6], but also their unusual effects induced by the Coulomb interaction [7–12].

Dirac electron systems in molecular conductors, such as α-(BEDT-TTF)$_2$I$_3$, provide suitable platforms for studying the effect of interaction because the electron hopping integrals between neighboring molecules are smaller than the on-site repulsive interactions reflecting the weak intermolecular coupling [13–19]. At high pressure, α-(BEDT-TTF)$_2$I$_3$ is a massless Dirac electron system. However, at low pressure, a charge-ordered state appears presumably due to nearest-neighbor Coulomb repulsions [20–22], where anomalous spin-charge separation on spin gaps [23,24] and transport phenomena occur [25–27]. In addition, the long-range Coulomb interaction reshapes the Dirac cone because of a logarithmic velocity renormalization, which induces an anomalous magnetic response [28–30]. Moreover, ferrimagnetism and spin-triplet excitonic fluctuations are observed [31,32].

The Dirac electron system in α-(BEDT-TTF)$_2$I$_3$ is two-dimensional [19] because it is a layered molecular conductor and the hopping of electrons from one conducting layer to the neighboring one over the insulating anion layer is incoherent. By contrast, if the electron hopping perpendicular to the main conducting layer were coherent, the Dirac point would be connected and draw lines (rings) in the three-dimensional momentum space, which are called the Dirac nodal lines (rings) [33–36].

Such kinds of Dirac nodal line (ring) systems have indeed been found in graphite [37], transition-metal monophosphates [38], Cu$_3$N [39], antiperovskites [40], perovskite iridates [41], and hexagonal pnictides with the composition CaAgX (X = P, As) [42], as well as in the single-component molecular conductors [Pd(dddt)$_2$] [43–50], [Pt(dmdt)$_2$] [51–55], and [Ni(dmdt)$_2$] [54,55].

The Dirac nodal line (ring) systems exhibit not only the properties in common with two-dimensional Dirac electron systems, e.g., the in-plane conductivity [51], but also the characteristic electronic properties such as nondispersive Landau levels [56], the Kondo effect [57], quasitopological electromagnetic responses [58], and edge magnetism [54] because of the three dimensionality. However, the electron correlation effects on the Fermi surface in the Dirac nodal line systems have not yet been elucidated.

The prime focus of this study is such a Dirac nodal line system in [M(dmdt)2] (M = Pt, Ni), which is a single-component molecular conductor that consists of the M(dmdt)$_2$ molecules, where the bracket [···] stands for a crystal. This material is a triclinic system, as shown in Fig. 1, and has space-inversion symmetry. One unit cell contains one M(dmdt)$_2$ molecule. In previous studies, the electronic properties of [M(dmdt)$_2$] were studied using density functional theory (DFT) and tight-binding models were constructed on the basis of the extended Hückel method and DFT [51–54]. These investigations showed that [M(dmdt)$_2$] is a Dirac nodal line system. Furthermore, electronic resistivity measurements using conventional four-probe methods were performed and showed that the resistivity of [M(dmdt)$_2$] hardly depends on the temperature
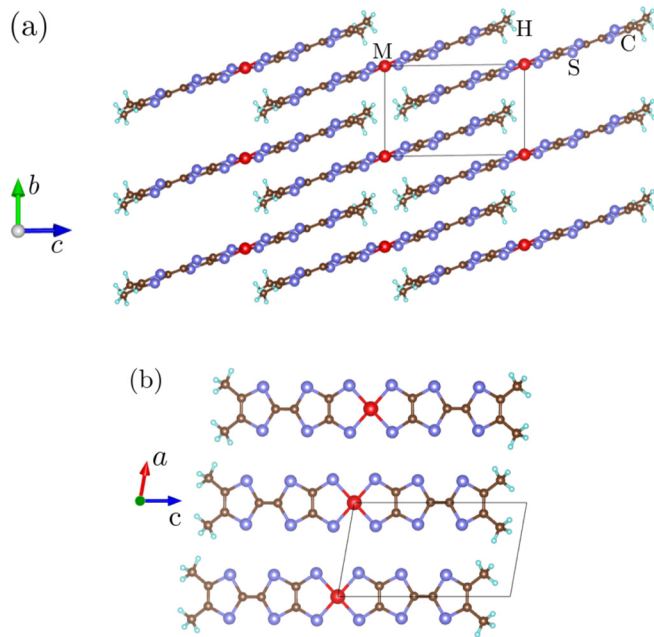
FIG. 1. (a) Crystal structure in the b–c plane of [M(dmdt)$_2$]. This material consists of M(dmdt)$_2$ molecules. (b) Crystal structure along the b-axis. The red, blue, brown, and cyan balls represent Ni, S, C, and H atoms, respectively. The black frames represent the unit cell.

(T), which is consistent with the property of the Dirac electron system [51]. That is the universal conductivity [59]. In addition, we previously suggested that the nesting between the Fermi arcs localized at the edge and the electronic correlation induce a helical spin density wave (SDW) at the edge [54].

Recently, the spin-lattice relaxation rate $1/T_1T$, probing the low-energy spin dynamics, and the Knight shift, scaling to the spin susceptibility, of [Ni(dmdt)$_2$] were observed in a ^{13}C nuclear magnetic resonance (^{13}C-NMR) experiment [60]. At high temperature, $1/T1T$ decreases with cooling and is almost proportional to T^2. However, at low temperature, it starts to increase with decreasing temperature and exhibits a peak structure at approximately 30 K. Meanwhile, the Knight shift is almost proportional to T because of the linear energy dispersion and does not increase. The mechanism of this anomalous temperature dependence of the spin fluctuations has not been elucidated.

In the present study, we theoretically investigate the electron correlation using the Fermi surface in [Ni(dmdt)$_2$] to elucidate the mechanism of this anomalous temperature dependence of the spin fluctuations. We calculate the spin susceptibility, Knight shift, and $1/T_1T$ using the random phase approximation (RPA) in a three-orbital Hubbard model describing [Ni(dmdt)$_2$], which is obtained using *ab initio* many-body perturbation theory calculations.

The electronic state of a molecular conductor is described by the molecular orbitals, which are linear combinations of the atomic orbitals in a molecule. The molecular orbital that has the highest energy and is fully occupied by electrons is called the highest-occupied molecular orbital (HOMO), whereas the one having the lowest energy with no electrons is called the lowest-unoccupied molecular orbital (LUMO). HOMO and

LUMO are also called frontier orbitals. The electronic states of single-component molecular conductors, e.g., [M(tmdt)$_2$] (M = Ni, Au, Cu) and [M(dmdt)$_2$] (M = Pt, Ni), are described by multiple molecular orbitals localized in a part of the molecule [53,54,61–63]. These molecular orbitals are the energy eigenstates obtained using first-principles calculations and are called "fragment orbitals." The fragment orbitals are transformed into HOMO and LUMO by a high-symmetry unitary transform.

Based on the band parameters determined from first-principle calculations, Seo *et al.* constructed a Hubbard model of [M(tmdt)$_2$](M=Ni, Au, Cu), which is described by the fragment orbitals [61,62]. The on-site repulsion acts between the same fragment orbitals that have spins of opposite signs, which is similar to the case of the present study. They investigated the ordered state by calculating the electron density and spin density using mean-field approximation. By contrast, in this study, we will investigate the spin fluctuations by calculating the spin susceptibility on the basis of RPA. Furthermore, we show that the idea of the fragment orbitals is important for the physical properties of the Dirac nodal line systems in the single-component molecular conductor. As the other previous studies of the fragment orbitals, some charge-transfer complexes such as (TTM-TTP)I$_3$ are also modeled by fragment orbitals [63,64].

We find that the $\mathbf{q} = \mathbf{0}$ spin fluctuations are enhanced in two out of the three fragment orbitals, while an enhancement at an incommensurate wave number vector develops in the third orbital. Detailed analysis showed that these $\mathbf{q} = \mathbf{0}$ spin fluctuations do not correspond to simple ferromagnetic fluctuations; rather, they are linked to intramolecular antiferromagnetic fluctuations. This implies that the spins of the fragment orbitals within the same molecule are inversely correlated. Further, $\mathbf{q} = \mathbf{0}$ implies a direct correlation of the spins between molecules. Using RPA, we determined that the $1/T_1T$ starts to increase at a low temperature by the $\mathbf{q} = \mathbf{0}$ spin fluctuations. By contrast, the Knight shift does not increase upon cooling because of the intramolecular antiferromagnetic fluctuations.

At high temperature, incommensurate spin fluctuations dominate the temperature dependence of $1/T_1T$. These magnetic responses are associated with the geometry of the Fermi surface and the characteristic wave functions of the n-orbital ($n \geqslant 3$) Dirac nodal line system. Thus, it is expected that other Dirac nodal line systems described by multiple-orbital models may have similar magnetic properties.

The remainder of this paper is organized as follows. In Sec. II, we introduce the spin susceptibility based on RPA and formulate $1/T_1T$ and the Knight shift. In Sec. III, we calculate the band structure, spin susceptibility, Knight shift, $1/T_1T$, and so on in the absence of interaction. In Sec. IV, we calculate the Stoner factor, Knight shift, and $1/T_1T$ in the presence of interaction by applying RPA to a Hubbard model. Section V draws conclusions.

II. FORMULATION

We calculate the spin susceptibility, which incorporates the electron correlation effect within perturbation theory to investigate the enhancement of spin fluctuations in [Ni(dmdt)$_2$].
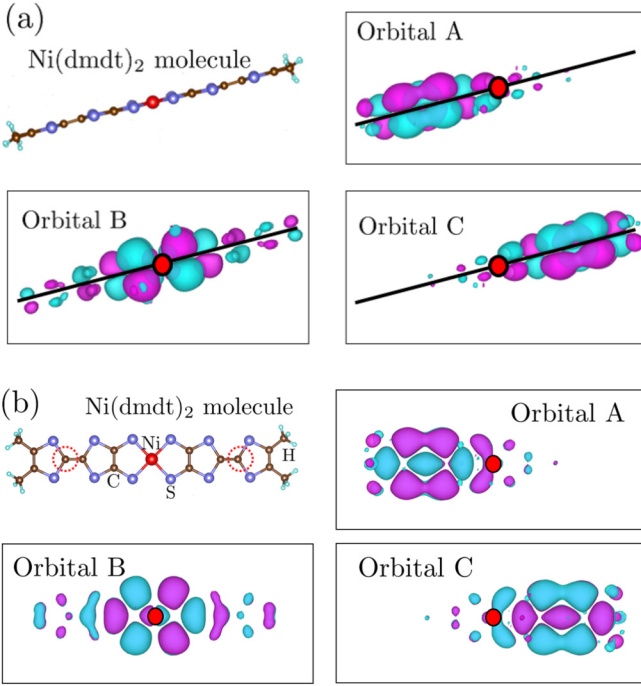
FIG. 2. Schematic of a Ni(dmdt)$_2$ molecule and the fragment orbitals A, B, and C. The red, blue, brown, and cyan balls represent Ni, S, C, and H atoms, respectively. The red dots in orbitals A, B, and C indicate the location of the Ni atom as a guide to the eye. (a) Side view of the molecule. The black solid line represents the Ni(dmdt)$_2$ molecule. (b) Vertical-axis view of the molecule. The red dashed circles indicate C atoms, which are replaced with ^{13}C in the ^{13}C-NMR experiment [60]. These figures are plotted by VESTA. Different colors represent different signs of the wave functions. The cut-off of the normalized wave functions is 0.01.

Furthermore, we calculate the Knight shift and the spin-lattice relaxation rate $1/T_1T$, which are the physical quantities observed using NMR. We apply RPA to the Hubbard model to calculate the spin susceptibility in [Ni(dmdt)$_2$]. Although calculations incorporating the self-energy, e.g., FLEX, are better approximations than RPA, RPA is more suitable for investigating spin fluctuations because the self-energy suppresses spin susceptibility.

The Hubbard Hamiltonian that we employ is given by

$$H = \sum_{\langle i,\alpha;j,\beta\rangle,\sigma} t_{i,\alpha;j,\beta} c^\dagger_{i,\alpha,\sigma} c_{j,\beta,\sigma} + \sum_{i,\alpha} U_\alpha n_{i,\alpha,\uparrow} n_{i,\alpha,\downarrow}, \quad (1)$$

where i and j are the unit-cell indices and σ is the spin index. Here, $t_{i,\alpha;j,\beta}$ is a transfer integral defined between the orbital α in the unit cell i and the orbital β in the cell j, and U_α represents the on-site repulsive interaction on the orbital α, with α and β standing for one of the three fragment orbitals in the unit cell (A, B, and C in Fig. 2). The indices α and β represent the three fragment orbitals A, B, and C. $\sum_{\langle...\rangle}$ represents a summation that runs only for the hoppings that have a larger energy scale than the cutoff (set to be 0.010 eV in this study).

The electronic states of [Ni(dmdt)$_2$] near the Fermi energy E_F are described by three fragment-decomposed Wannier

TABLE I. Transfer integrals and site potential of [Ni(dmdt)$_2$].

Transfer integrals (eV)	
t_1	−0.2372
t_2	−0.1840
t_3	−0.2080
t_4	0.0302
t_5	0.0326
t_6	−0.0389
t_7	0.0103
t_8	−0.0144
t_9	−0.0140
t_{10}	−0.0541
t_{11}	−0.0534
t_{12}	0.0116
Site potential (eV)	
Δ	0.0429

orbitals (fragment orbitals) dubbed orbitals A, B, and C as illustrated in Fig. 2. They are obtained using Wannier fitting to three isolated energy bands near E_F, which were previously obtained using first-principles calculations [54].

The Wannier fitting and first-principles calculations were performed using the programs RESPACK [65] and QUANTUM ESPRESSO [66], respectively [54]. RESPACK was also used for calculating the Coulomb interaction and other factors. Further, QUANTUM ESPRESSO was used for first-principles calculations based on the pseudopotential method. Figures 2(a) and 2(b) show a side and vertical-axis view, respectively, of the molecule. Orbital B in Fig. 2(a) may look like a d orbital, but is a p orbital of the S atoms, as is evident from Fig. 2(b). The d orbital of Ni is localized near the Ni atom, and its contribution to the orbital B is small. Orbitals A and C have p-orbital-like shapes and are equivalent because of space-inversion symmetry. In the present study, we assume that these three fragment orbitals sit in the same molecule and in the same unit cell.

By performing a Fourier transform, the Hamiltonian [Eq. (1)] is rewritten as

$$H = \sum_{\mathbf{k},\alpha,\beta,\sigma} H^0_{\alpha\beta,\sigma}(\mathbf{k}) c^\dagger_{\mathbf{k},\alpha,\sigma} c_{\mathbf{k},\beta,\sigma}$$
$$+ \frac{1}{N_L} \sum_{\mathbf{k},\mathbf{k}',\mathbf{q},\alpha} U_{\alpha\alpha} c^\dagger_{\mathbf{k}+\mathbf{q},\alpha,\uparrow} c^\dagger_{\mathbf{k}'-\mathbf{q},\alpha,\downarrow} c_{\mathbf{k}',\alpha,\downarrow} c_{\mathbf{k},\alpha,\uparrow}, \quad (2)$$

where $\mathbf{k}$, $\mathbf{k}'$, and $\mathbf{q}$ are the wave-number vectors. N_L is the number of the unit cells in the system. The first term corresponds to the unperturbed Hamiltonian, and the second term is treated as a perturbed Hamiltonian. Here, $H^0_{\alpha\beta,\sigma}(\mathbf{k})$ is defined as

$$H^0_{\alpha\beta,\sigma}(\mathbf{k}) = \sum_{\langle\delta\rangle} t_{\alpha\beta,\sigma,\delta} e^{i\mathbf{k}\cdot\delta}, \quad (3)$$

where δ is a lattice vector connecting the neighbor unit cell. Further, $t_{\alpha\beta,\sigma,\delta}$ is the transfer integral between the fragment orbitals α and β, which are separated by the lattice vector δ and have the spin σ. We allot $t_{\alpha\beta,\sigma,\delta}$ to the transfer integrals $t_1, t_2, \ldots, t_{12}$ and the site potential Δ in Table I, where
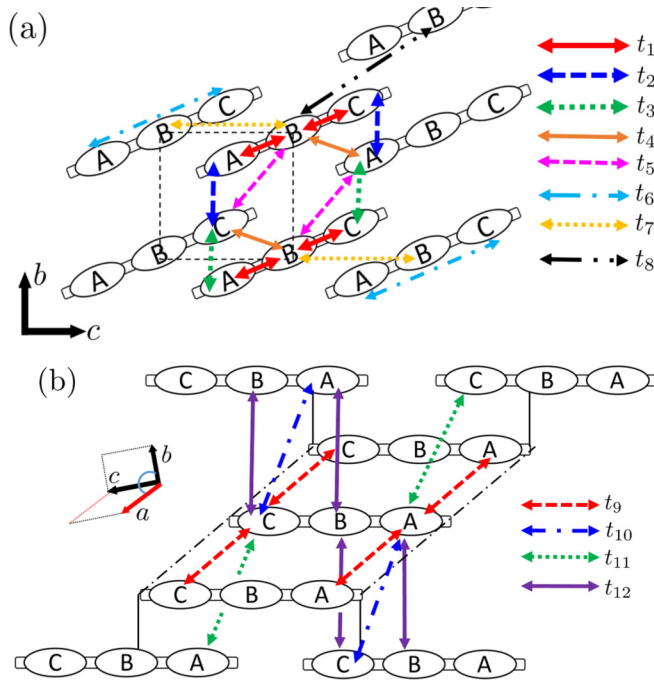
FIG. 3. Hopping networks between fragment orbitals in tight-binding model of [Ni(dmdt)2]. (a) Schematic illustration of the 2D network of the transfer integrals (shown by double-headed arrows) in the crystalline bc-plane. The dashed square stands for the unit cell. (b) Schematic illustration of the 3D hopping network including the transfer integrals along the a-direction. The black chain lines and vertical bold lines in (b) are guides to the eyes: The first lines are parallel to the a-direction, while the second lines connect the molecules in the same bc-plane.

$\Delta \equiv t_{BB,\sigma,\mathbf{0}} - t_{AA,\sigma,\mathbf{0}}$. Note that these transfer integrals were obtained from the Wannier fitting. In additions, we omit the small hoppings whose sizes are less than a cutoff energy of 0.010 eV to make the analysis simple (see Fig. 3 for the schematic illustration of such a hopping network). Note that t_1 connects the nearest-neighbor fragment orbitals within a molecule, while $t_2, t_3,..., t_8$ connect those between molecules in the crystalline b–c plane, which corresponds to the k_b–k_c plane in momentum space, where the Dirac cones exist. We point out that t_1, t_2, and t_3 are the three essential transfer integrals that are needed to create the Dirac cones, while t_9 creates Fermi surfaces, and t_{10}, t_{11}, and t_{12} wind the Dirac nodal lines. Previously, we calculated some quantities of [M(dmdt)$_2$] (M = Pt, Ni) considering the spin-orbit interaction (SOI) as a parameter. There, we found that the SOI can reduce the Fermi surface in the bulk and induce helical edge modes [53,54]. However, because the energy scale of SOI in this material ($\sim$0.0016 eV) seems to be considerably smaller than the energy scale of the Fermi surface ($\sim$0.01 eV) [54], in reality SOI should not be large enough to significantly reduce the size of the Fermi surface. Therefore, we will omit the influence of SOI on the Knight shift and $1/T_1T$.

From the definition in Eq. (3), $H^0_{\alpha\beta,\sigma}(\mathbf{k})$ are expressed by the following equations:

$$
\begin{aligned}
H^0_{AA,\sigma}(\mathbf{k}) &= 2t_9 \cos k_a, \\
H^0_{AB,\sigma}(\mathbf{k}) &= t_{12}e^{i(-k_a+k_b+k_c)} + t_1 \\
&\quad + t_5 e^{i(k_b+k_c)} + t_4 e^{ik_c}, \\
H^0_{AC,\sigma}(\mathbf{k}) &= t_{10}e^{i(-k_a+k_b+k_c)} + t_{11}e^{i(k_a+k_c)} + t_6 \\
&\quad + t_3 e^{ik_c} + t_2 e^{i(k_b+k_c)}, \\
H^0_{BB,\sigma}(\mathbf{k}) &= \Delta + 2t_7 \cos(k_b+k_c) + 2t_8 \cos k_c, \\
H^0_{BC,\sigma}(\mathbf{k}) &= t_{12}e^{i(-k_a+k_b+k_c)} + t_1 \\
&\quad + t_5 e^{i(k_b+k_c)} + t_4 e^{ik_c}, \\
H^0_{CC,\sigma}(\mathbf{k}) &= 2t_9 \cos k_a.
\end{aligned}
\tag{4}
$$

Here, for simplicity, we set all the lattice constants to be unity. Two of the three bands for which we performed Wannier fitting are occupied [53]. Thus, the tight-binding model obtained using the Wannier fitting is also 2/3 filling. The unperturbed Hamiltonian $\hat{H}^0_\sigma(\mathbf{k})$ satisfies the eigenvalue equation

$$
\hat{H}^0_\sigma(\mathbf{k}) |\mathbf{k}, n, \sigma\rangle = E_{n,\sigma}(\mathbf{k}) |\mathbf{k}, n, \sigma\rangle,
\tag{5}
$$

$$
|\mathbf{k}, n, \sigma\rangle = \begin{pmatrix} d_{A,n,\sigma}(\mathbf{k}) \\ d_{B,n,\sigma}(\mathbf{k}) \\ d_{C,n,\sigma}(\mathbf{k}), \end{pmatrix},
\tag{6}
$$

where $E_{n,\sigma}(\mathbf{k})$ is the eigenvalue and $|\mathbf{k}, n, \sigma\rangle$ is the eigenvector; n is the band index; and $d_{\alpha,n,\sigma}(\mathbf{k})$ denotes the wave functions. $\hat{H}^0_\sigma(\mathbf{k})$ in Eq. (5) consists of the matrix elements $H^0_{\alpha\beta,\sigma}(\mathbf{k})$ in Eqs. (2) and (4). Reflecting the 2/3-filling, the chemical potential μ is determined by

$$
\frac{1}{N_L} \sum_{\mathbf{k},n,\sigma} f_{\mathbf{k},n,\sigma} = 4,
\tag{7}
$$

$$
\epsilon_{\mathbf{k},n,\sigma}(\mathbf{k}) \equiv E_{n,\sigma}(\mathbf{k}) - \mu,
\tag{8}
$$

$f_{\mathbf{k},n,\sigma} = 1/[1 + \exp(\epsilon_{\mathbf{k},n,\sigma}/T)]$ is the Fermi distribution function, and we have $\mu = E_F$ at $T = 0$.

As to the second term in the Hamiltonian Eq. (2), we introduce the on-site repulsive interaction $U_{\alpha\alpha}$ defined on the fragment orbital α, which is defined as the diagonal element of the interaction matrix as follows:

$$
\begin{aligned}
\hat{U} &= \begin{pmatrix} U_{AA} & 0 & 0 \\ 0 & U_{BB} & 0 \\ 0 & 0 & U_{CC} \end{pmatrix} \\
&= \begin{pmatrix} \lambda U & 0 & 0 \\ 0 & U & 0 \\ 0 & 0 & \lambda U \end{pmatrix}.
\end{aligned}
\tag{9}
$$

Here, because of the inversion symmetry, we have $U_{AA} = U_{CC}$, and we use the relative size of U_{AA} to U_{BB}, $\lambda = U_{AA}/U_{BB}$, as a control parameter of this model. According to RESPACK, we found $U = 6.72$ eV and $\lambda = 0.79$ in the unscreened case, and $U = 2.68$ eV and $\lambda = 0.95$ in the screened case. In this study, we set $\lambda = 0.95$ and use a value of U less than 2.68 eV because $\hat{U}$ tends to be overestimated in RPA.

The longitudinal and transverse spin susceptibilities are defined as follows [67] :

$$\hat{\chi}^{zz}(\mathbf{q}, i\omega_l) \equiv \frac{1}{2} \int_0^{1/T} d\tau\, e^{i\omega_l\tau} \langle T_\tau \hat{S}_\mathbf{q}^z(\tau)\hat{S}_{-\mathbf{q}}^z(0)\rangle, \quad (10)$$

$$\hat{S}_\mathbf{q}^z = \frac{1}{N_L}\sum_\mathbf{k} \left(\hat{c}_{\mathbf{k+q},\uparrow}^\dagger \hat{c}_{\mathbf{k},\uparrow} - \hat{c}_{\mathbf{k+q},\downarrow}^\dagger \hat{c}_{\mathbf{k},\downarrow}\right), \quad (11)$$

$$\hat{\chi}^{\pm}(\mathbf{q}, i\omega_l) \equiv \int_0^{1/T} d\tau\, e^{i\omega_l\tau} \langle T_\tau \hat{S}_\mathbf{q}^+(\tau)\hat{S}_{-\mathbf{q}}^-(0)\rangle, \quad (12)$$

$$\hat{S}_\mathbf{q}^+ = \frac{1}{N_L}\sum_\mathbf{k} \hat{c}_{\mathbf{k},\uparrow}^\dagger \hat{c}_{\mathbf{k+q},\downarrow}, \quad (13)$$

$$\hat{S}_{-\mathbf{q}}^- = \frac{1}{N_L}\sum_\mathbf{k} \hat{c}_{\mathbf{k+q},\downarrow}^\dagger \hat{c}_{\mathbf{k},\uparrow}. \quad (14)$$

Here, $i\omega_l = 2il\pi T$ ($l \in \mathbf{N}$) is the Matsubara frequency and τ is the imaginary time. $\hat{S}_\mathbf{q}^{zz}$, $\hat{S}_\mathbf{q}^+$, and $\hat{S}_\mathbf{q}^-$ are the spin operators. $\hat{S}_\mathbf{q}^{zz}(\tau)$, $\hat{S}_\mathbf{q}^+(\tau)$, and $\hat{S}_\mathbf{q}^-(\tau)$ are described in the Heisenberg picture. The spin susceptibility is the proportionality coefficient of the magnetization to the infinitesimal magnetic field. It represents the degree of the "spin fluctuations" because spins in the system sensitively respond to the infinitesimal magnetic field when spin susceptibility is large.

By performing a perturbation expansion of Eqs. (10) and (12), we obtain the noninteracting longitudinal spin susceptibility $\hat{\chi}^{zz,0}(\mathbf{q}, i\omega_l)$ and noninteracting transverse spin susceptibility $\hat{\chi}^{\pm,0}(\mathbf{q}, i\omega_l)$ as the zeroth-order perturbation terms. In this study, SU(2) symmetry is protected. Therefore, we define $\hat{\chi}^{zz,0}(\mathbf{q}, i\omega_l) = \hat{\chi}^{\pm,0}(\mathbf{q}, i\omega_l) \equiv \hat{\chi}^0(\mathbf{q}, i\omega_l)$. Its matrix elements are written as

$$\chi_{\alpha\beta}^0(\mathbf{q}, i\omega_l) = -\frac{T}{N_L}\sum_{\mathbf{k},m} G_{\alpha\beta}^0(\mathbf{k+q}, i\tilde{\omega}_m + i\omega_l) G_{\beta\alpha}^0(\mathbf{k}, i\tilde{\omega}_m), \quad (15)$$

$$G_{\alpha\beta,\sigma}^0(\mathbf{k}, i\tilde{\omega}_l) = \sum_n d_{\alpha,n,\sigma}(\mathbf{k})d_{\beta,n,\sigma}^*(\mathbf{k}) \frac{1}{i\tilde{\omega}_l - \epsilon_{\mathbf{k},n,\sigma}}. \quad (16)$$

Equation (16) expresses the matrix elements of the noninteracting Green's function. $i\tilde{\omega}_l = (2l+1)i\pi T$ is the Matsubara frequency of the fermions. The spin index σ is omitted in Eq. (15) because we have $\epsilon_{\mathbf{k},n,\uparrow} = \epsilon_{\mathbf{k},n,\downarrow}$ in Eq. (16). The longitudinal and transverse spin susceptibilities in RPA are represented by the Feynman diagrams shown in Fig. 4. The first terms in the right-hand sides of Figs. 4(a) and 4(b) correspond to the terms $\hat{\chi}^{zz,0}(\mathbf{q}, i\omega_l) = \hat{\chi}^{\pm,0}(\mathbf{q}, i\omega_l) = \hat{\chi}^0(\mathbf{q}, i\omega_l)$ [Eq. (15)]. Because the interacting longitudinal and transverse spin susceptibilities are represented by summations of the series of $\hat{U}\hat{\chi}^0(\mathbf{q}, i\omega_l)$ in RPA, they are written as

$$\hat{\chi}^{zz,s}(\mathbf{q}, i\omega_l) = \hat{\chi}^{\pm,s}(\mathbf{q}, i\omega_l) \equiv \hat{\chi}^s(\mathbf{q}, i\omega_l)$$
$$= \hat{\chi}^0(\mathbf{q}, i\omega_l)[\hat{I} - \hat{U}\hat{\chi}^0(\mathbf{q}, i\omega_l)]^{-1}, \quad (17)$$

where $\hat{I}$ is the unit matrix.

Here we introduce the Stoner factor $\xi_s(\mathbf{q})$ representing the degree of enhancement of the spin fluctuations. The Stoner factor $\xi_s(\mathbf{q})$ is defined as the maximum eigenvalue of $\hat{U}\hat{\chi}^0(\mathbf{q}, 0)$. The relation between $\xi_s(\mathbf{q})$ and $\hat{\chi}^s(\mathbf{q}, 0)$ in the
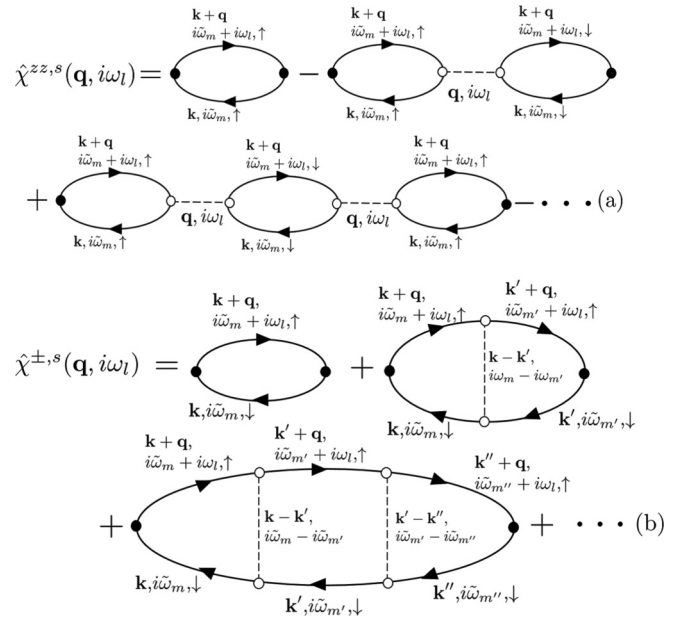

FIG. 4. (a) Feynman diagram of $\hat{\chi}^{zz,s}(\mathbf{q}, i\omega_l)$. (b) Feynman diagram of $\hat{\chi}^{\pm,s}(\mathbf{q}, i\omega_l)$. The solid lines represent the noninteracting Green's functions, which describe the quasiparticles. The dashed lines represent the interactions. The open circles are the vertexes connecting the noninteracting Green's functions and the interaction. The black dots represent the spin operators.

three-orbital model is given by

$$\hat{\chi}^s(\mathbf{q}, 0) = \frac{1}{[1 - \xi_s(\mathbf{q})]} \frac{\hat{\chi}^0(\mathbf{q}, 0)\hat{P}(\mathbf{q})}{[1 - \phi_1(\mathbf{q})][1 - \phi_2(\mathbf{q})]}, \quad (18)$$

where $\xi_s(\mathbf{q})$, $\phi_1(\mathbf{q})$, and $\phi_2(\mathbf{q})$ are the maximum and other eigenvalues of $\hat{U}\hat{\chi}^0(\mathbf{q}, 0)$. $\hat{P}(\mathbf{q})$ is the adjugate matrix of $\hat{I} - \hat{U}\hat{\chi}^0(\mathbf{q}, 0)$. The eigenvalues of $\hat{U}\hat{\chi}^0(\mathbf{q}, 0)$ are smaller than 1 in the paramagnetic regime. When $\xi_s(\mathbf{q}) \to 1$, the spin susceptibility $\hat{\chi}^s(\mathbf{q}, 0)$ diverges and induces a magnetic order, corresponding to the wave number $\mathbf{q}$.

Within the framework of linear response theory, the Knight shift, K, and the spin-lattice relaxation rate, $(1/T_1T)$, for the orbital α are given by

$$K_\alpha \propto \sum_\beta \mathrm{Re}\big[\chi_{\alpha\beta}^{zz}(\mathbf{0}, 0)\big], \quad (19)$$

$$(1/T_1T)_\alpha \propto \lim_{\omega\to+0}\left[\frac{1}{N_L}\sum_\mathbf{q} \frac{\mathrm{Im}\chi_{\alpha\alpha}^{\pm}(\mathbf{q}, \omega)}{\omega}\right]. \quad (20)$$

Here, note that Eq. (17) is satisfied. According to Eqs. (18) and (20), all the $\mathbf{q}$ components for which $\xi_s(\mathbf{q})$ becomes close to unity make a dominant contribution to $1/T_1T$ because they lead to a large value in the spin susceptibility. By contrast, the Knight shift is solely affected by the $\mathbf{q} = \mathbf{0}$ component that satisfies $\xi_s(\mathbf{q}) \sim 1$ [see Eq. (19)].

Because the spin susceptibility in the real-frequency representation $\hat{\chi}^s(\mathbf{q}, \omega)$ is necessary for $1/T_1T$, we obtain $\hat{\chi}^s(\mathbf{q}, \omega)$ by performing an analytic continuation of Eqs. (17). In this way, we use the real-frequency representation depending on the physical quantities.
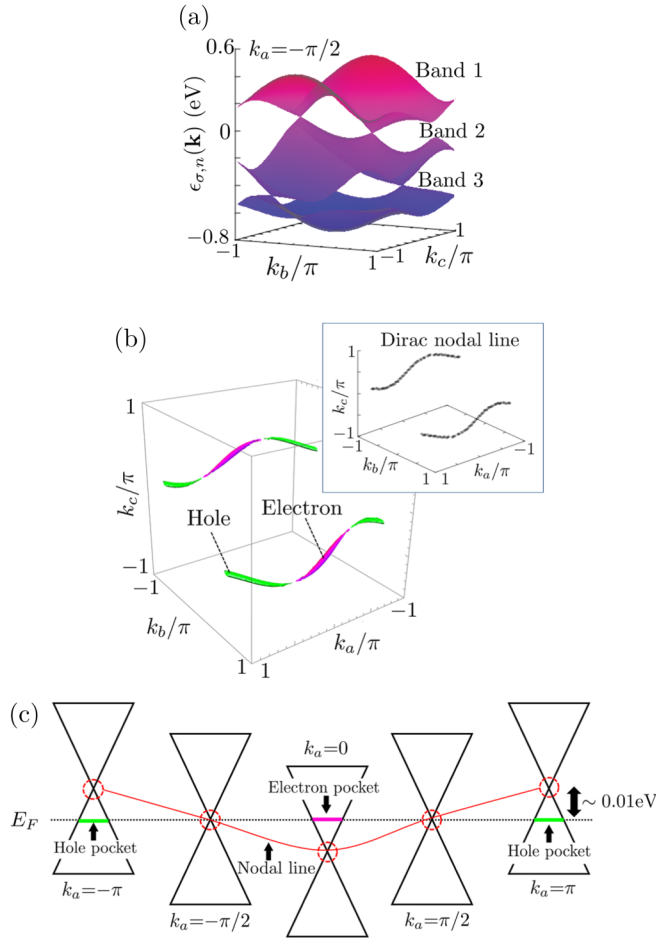
FIG. 5. (a) Energy dispersion of [Ni(dmdt)$_2$] in the k_b–k_c plane, where $k_a = -\pi/2$. Dirac cones exist between each pair of bands. Those between bands 1 and 2 draw the Dirac nodal line. (b) Fermi surface in the first Brillouin zone. The electron and hole pockets are drawn in magenta and green, respectively. The inset shows the Dirac nodal line in the first Brillouin zone. (c) Schematic of the relationship among the Dirac nodal line, Fermi surface, and wave number k_a. The red curved line shows the Dirac nodal line. The dotted transverse line shows E_F.

III. RESULT IN THE ABSENCE OF U

In this section, we calculate the electronic state, spin susceptibility, Knight shift, and $1/T_1T$ in the absence of the repulsive interaction U. Further, we find that the spin susceptibility in [Ni(dmdt)$_2$] greatly depends on the fragment orbitals and will explain the relationship between the spin susceptibilities and the wave functions.

A. Electronic state and spin susceptibility in the absence of U

We first calculate the energy dispersion of [Ni(dmdt)$_2$] by diagonalizing the unperturbed Hamiltonian $\hat{H}_\sigma^0(\mathbf{k})$ in Eq. (5). The resulting energy bands are depicted in Fig. 5(a), where the dispersion seen in the k_b–k_c plane at $k_a = -\pi/2$ is shown. Inside the two-dimensional (2D) first Brillouin zone, two pairs of gapless Dirac cones appear between the first and second top bands near E_F [the Band 1 and 2 in Fig. 5(a), where E_F is chosen as the energy origin] and between the second and
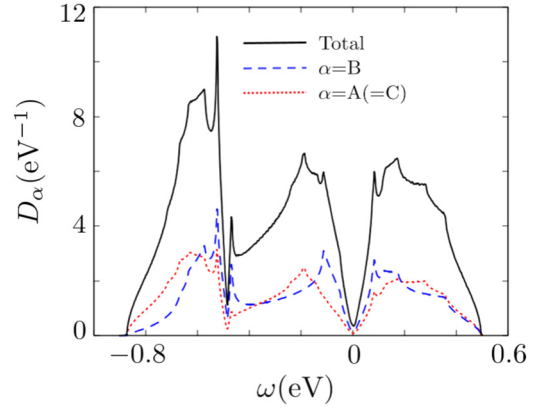

FIG. 6. The local density of state $D_\alpha(\omega)$ for the fragment orbital $\alpha = $ A, B, and C in the unit cell of [Ni(dmdt)$_2$]. The red dotted and blue dashed lines show $D_A(\omega)[=D_C(\omega)]$ and $D_B(\omega)$, respectively. The black solid line shows the total density of states $D_{\text{tot}}(\omega) = D_A(\omega) + D_B(\omega) + D_C(\omega)$. The integral value of $D_{\text{tot}}(\omega)$ over ω is equal to 6 due to the three orbitals and the spins. Its unit is the number of electrons.

third bands rather beneath E_F (the Bands 2 and 3), where these band-crossing points are protected by space-inversion symmetry.

Dirac points between bands 1 and 2 in the k_b–k_c plane draw the Dirac nodal lines in the k_a direction. The inset of Fig. 5(b) shows the Dirac nodal line in the first Brillouin zone. Upon changing the momentum along the k_a direction, the positions of the Dirac points near E_F move in the k_b–k_c plane and eventually form a pair of so-called Dirac nodal lines in the three-dimensional (3D) Brillouin zone [see the inset of Fig. 5(b)]. The band-crossing points accordingly move up and down across E_F with changing the value of k_a as illustrated in Fig. 5(c), which generates electron and hole pockets around these nodal lines [see Fig. 5(b), where the electron and hole pockets are illustrated as thin magenta and green strips, respectively]. Figure 5(b) shows the Fermi surface in [Ni(dmdt)$_2$]. The energy scale of such Fermi pockets is approximately 0.010 eV.

The corresponding density of states (DOS), $D_{\text{tot}}(\omega)$, was also calculated, which is given by a sum of a fragment-orbital dependent DOS, $D_\alpha(\omega)$ [α=A(=C) and B], that is given by

$$D_\alpha(\omega) = -\frac{1}{\pi N_L} \sum_{\mathbf{k},\sigma} \text{Im} G_{\alpha\alpha,\sigma}^{R,0}(\mathbf{k}, \omega), \qquad (21)$$

$$G_{\alpha\beta,\sigma}^{R,0}(\mathbf{k}, \omega) = \sum_n d_{\alpha,n,\sigma}(\mathbf{k}) d_{\beta,n,\sigma}^*(\mathbf{k}) \frac{1}{\omega - \epsilon_{\mathbf{k},n,\sigma} + i\eta}. \qquad (22)$$

Here, $\hat{G}^{R,0}(\mathbf{k}, \omega)$ is the noninteracting retarded Green's function, where $\eta = +0$. The resulting $D_{\text{tot}}(\omega)$ and $D_\alpha(\omega)$ are depicted in Fig. 6. Note that the DOS has linear ω dependence near E_F (corresponding to $\omega = 0$ in Fig. 6) because the energy dispersion of this system near E_F is close to that of a two-dimensional Dirac electron system, and the three-dimensional effect is only an addition of a small dispersion along a k_a direction. The finite DOS at E_F in this material is ascribed to the presence of the Fermi pockets induced by that k_a-axis dispersion.
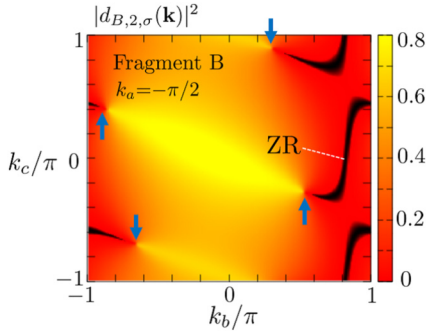
FIG. 7. Wave function of orbital B in band 2, $|d_{B,2,\sigma}(\mathbf{k})|^2$, in the k_b–k_c plane, where $k_a = -\pi/2$. The up arrows indicate the corresponding positions of the Dirac points formed between the Bands 1 and 2 in Fig. 5(a), while the down arrows indicate those between the Bands 2 and 3. The color bar represents the magnitude of $|d_{B,2,\sigma}(\mathbf{k})|^2$.

Before moving to the analysis of the spin susceptibility, further comments are needed on the fragment-orbital-dependent characters of this system. Figure 7 shows the momentum dependence of the squared wave function for the orbital B projected onto the second top band [Band 2 in Fig. 5(a)], $|d_{B,2,\sigma}(\mathbf{k})|^2$, plotted as a function of k_b and k_c at $k_a = -\pi/2$. Notably, the line segments that connect the positions of these Dirac points (illustrated with black lines in Fig. 7) have a vanishing amplitude, $|d_{B,2,\sigma}(\mathbf{k})|^2 = 0$, which we call the "zero region" (ZR) in this paper. By contrast, the wave functions of the orbitals A and C do not have such ZR. The presence of a similar ZR was previously found in other n-band ($n \geqslant 3$) Dirac electron systems, such as the organic conductors α-(BEDT-TTF)$_2$I$_3$ ($n = 4$) [30].

Second, we calculate the noninteracting spin susceptibility $\hat{\chi}^0(\mathbf{q}, \omega)$ to elucidate spin fluctuations, which can be enhanced in this material. Figures 8(a), 8(b), 8(c), and 8(d) show the diagonal elements of the noninteracting spin susceptibility $\chi^0_{AA}(\mathbf{q}, 0)$, $\chi^0_{BB}(\mathbf{q}, 0)$, Im[$\chi^0_{AA}(\mathbf{q}, \omega_0)$], and Im[$\chi^0_{BB}(\mathbf{q}, \omega_0)$], respectively, at $T = 0.003$ eV. These quantities slightly increase with raising temperature for any $\mathbf{q} = \mathbf{0}$ values, while the magnitude relation $\chi^0_{AA}(\mathbf{q} \sim \mathbf{0}, 0) < \chi^0_{BB}(\mathbf{q} \sim \mathbf{Q}, 0)$ and Im[$\chi^0_{AA}(\mathbf{q} \sim \mathbf{0}, \omega_0)$] > Im[$\chi^0_{BB}(\mathbf{q} \sim \mathbf{Q}, \omega_0)$] do not change with temperature. Here, $\chi^0_{\alpha\alpha}(\mathbf{q}, 0)$ is a real number. We set $\omega_0 = 0.001$ eV because the imaginary part of the spin susceptibility at the infinitesimal frequency is essential to solve Eq. (20). One of q_a, q_b, and q_c must be fixed to show the spin susceptibilities in the three-dimensional figures. We fix $q_a = 0$ in Figs. 8(a) and 8(c) and $q_a = 0.2\pi$ in Figs. 8(b) and 8(d) because $\chi^0_{AA}(\mathbf{q}, 0)$ and $\chi^0_{BB}(\mathbf{q}, 0)$ have the maximum value at the commensurate wave number $\mathbf{q} = \mathbf{0}$ and the incommensurate wave number $\mathbf{q} = \mathbf{Q} = (0.20\pi, 0.73\pi, 0.58\pi)$ at $T = 0.003$ eV, respectively. We define $\mathbf{Q}$ as the wave number at which $\chi^0_{BB}(\mathbf{q}, 0)$ has the maximum value. Further, $\mathbf{Q}$ varies slightly with temperature. $\chi^0_{CC}(\mathbf{q}, \omega)$ is equivalent to $\chi^0_{AA}(\mathbf{q}, \omega)$ owing to space-inversion symmetry. In Figs. 8(a) and 8(c), $\chi^0_{AA}(\mathbf{q}, 0)$ and Im[$\chi^0_{AA}(\mathbf{q}, \omega_0)$] have their maximum value at $\mathbf{q} = \mathbf{0}$. In Figs. 8(b) and 8(d), $\chi^0_{BB}(\mathbf{q}, 0)$ and Im[$\chi^0_{BB}(\mathbf{q}, \omega_0)$] have their maximum value at $\mathbf{q} = \mathbf{Q}$. In addition, Im[$\chi^0_{BB}(\mathbf{q}, \omega_0)$] has some peaks other than that at $\mathbf{q} = \mathbf{Q}$.

The difference between $\chi^0_{AA}(\mathbf{q}, 0)$ and $\chi^0_{BB}(\mathbf{q}, 0)$ implies that [Ni(dmdt)$_2$] has two candidates for magnetic order that
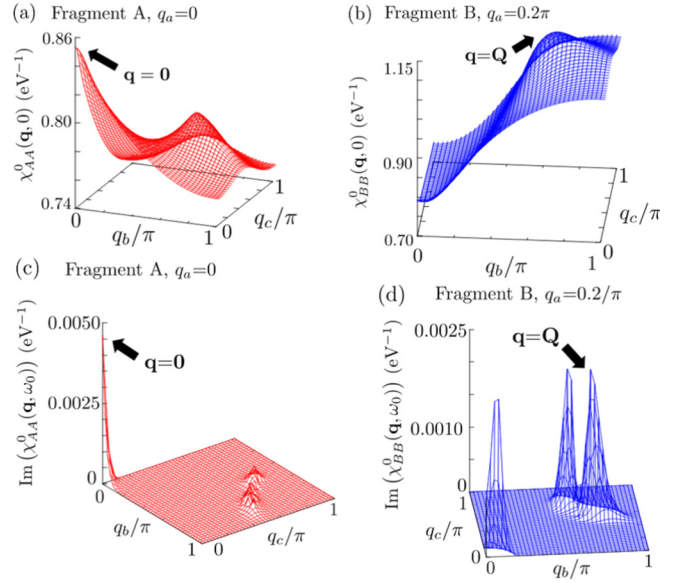

FIG. 8. The momentum dependencies of the diagonal elements of the spin susceptibility in the absence of U. (a) $\chi^0_{AA}(\mathbf{q}, 0)$ in the q_b–q_c plane, where $q_a = 0$. (b) $\chi^0_{BB}(\mathbf{q}, 0)$ in the q_b–q_c plane, where $q_a = 0.2\pi$. (c) Im[$\chi^0_{AA}(\mathbf{q}, \omega_0)$] in the q_b–q_c plane, where $q_a = 0$. (d) Im[$\chi^0_{BB}(\mathbf{q}, \omega_0)$] in the q_b–q_c plane, where $q_a = 0.2\pi$. The temperature $T = 0.003$ eV.

can be induced in the bulk. They are the $\mathbf{q} = \mathbf{0}$ magnetic order and SDW. To explain the mechanism of the fragment-orbital-dependent spin susceptibility, we calculate the spectral weights on the Fermi surface. The spectral weight is given by

$$\rho_\alpha(\mathbf{k}, \omega) = -\frac{1}{\pi} \mathrm{Im} G^{R,0}_{\alpha\alpha}(\mathbf{k}, \omega). \quad (23)$$

The spin index σ is omitted in Eq. (23), and $\mathbf{k} = (k_a, k_b, k_c)$ is the wave number. Equation (23) with $\omega = 0$ yields the spectral weight at E_F. The spectral weight shows the weights of the respective fragment orbitals for the energy ω and the wave number $\mathbf{k}$ because $G^{R,0}_{\alpha\alpha}(\mathbf{k}, \omega)$ in Eq. (23) contains the absolute square of the wave function $|d_{\alpha,n}(\mathbf{k})|^2$. Furthermore, the relationship $\frac{1}{N_L} \sum_{\mathbf{k}} \rho_\alpha(\mathbf{k}, \omega) = D_\alpha(\omega)$ is satisfied. Figures 9(a) and 9(b) show the spectral weight on the cross-section where the Fermi surface in Fig. 5(b) is cut on the $k_a = \pi$ plane, which corresponds to the hole pocket. We set $k_a = \pi$ because
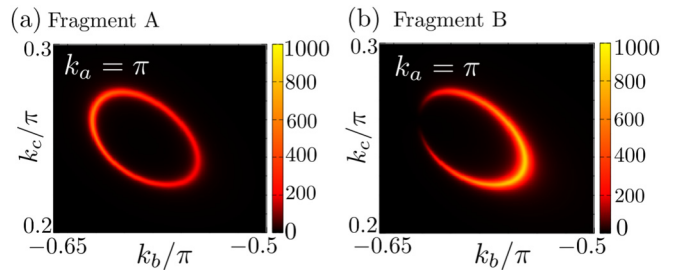

FIG. 9. (a) Spectral weight $\rho_A(\mathbf{k}, 0)$. It is not zero on the Fermi surface. (b) Spectral weight $\rho_B(\mathbf{k}, 0)$. A part of it is zero because of a ZR. In the both figures, $k_a = \pi$, $-0.65\pi < k_b < -0.50\pi$, and $0.20\pi < k_c < 0.30\pi$. Color bars represent the magnitude of the spectral weight $\rho_\alpha(\pi, k_b, k_c, 0)$. The yellow region indicates that the spectral weight at E_F is high.
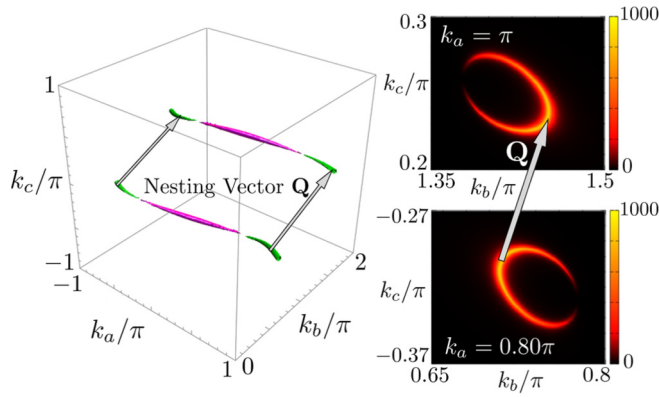
FIG. 10. Nesting vector **Q** in the momentum space. **Q** connects the regions where the spectral weight of orbital B is high (in the right figure). Color bars represent the magnitude of the spectral weight $\rho_B(\pi, k_b, k_c, 0)$. The electron and hole pockets are drawn in magenta and green, respectively (in the left figure).

the hole pockets are important for $\chi^0_{BB}(\mathbf{q}, 0)$, as we discuss below. Figures 9(a) and 9(b), respectively, show $\rho_A(\mathbf{k}, 0)$ and $\rho_B(\mathbf{k}, 0)$ in the k_b–k_c plane. In both figures, $-0.65\pi < k_b < -0.50\pi$ and $0.20\pi < k_c < 0.30\pi$. The spectral weight of A is not zero on the Fermi surface, but that of B has the appearance of a crescent moon because of a ZR. This difference in spectral weights results in the fragment-orbital-dependent spin susceptibilities.

After performing summation over $i\omega_m$ in Eq. (15), the noninteracting spin susceptibility is written as

$$\chi^0_{\alpha,\beta}(\mathbf{q}, i\omega_l) = -\frac{1}{N_L} \sum_{\mathbf{k},m,n} \frac{f_{\mathbf{k}+\mathbf{q},m} - f_{\mathbf{k},n}}{\epsilon_{\mathbf{k}+\mathbf{q},m} - \epsilon_{\mathbf{k},n} - i\omega_l}$$
$$\times d_{\alpha,m}(\mathbf{k}+\mathbf{q})d^*_{\beta,m}(\mathbf{k}+\mathbf{q})d_{\beta,n}(\mathbf{k})d^*_{\alpha,n}(\mathbf{k}),$$
(24)

where the spin index σ is omitted. The terms in which the denominator is close to 0 and the numerator is close to 1 in Eq. (24) contribute to $\chi^0_{\alpha\beta}(\mathbf{q}, 0)$. Such terms are given by the wave number $\mathbf{k} + \mathbf{q}$ and $\mathbf{k}$ near the Fermi surface. Thus, the vector $\mathbf{q}$ connecting the Fermi surface is important for the spin susceptibility. This wave number is called the nesting vector. $\mathbf{q} = \mathbf{Q}$ in Fig. 8 corresponds to the nesting vector $\mathbf{Q}$ in Fig. 10. $\mathbf{q} = \mathbf{Q}$ connects the regions where the spectral weight of orbital B is high on the hole pockets. $\mathbf{Q}$ is the wave number at which $\chi^0_{BB}(\mathbf{q}, 0)$ has the maximum value. The nesting between the electron pockets is relatively weaker than that between the hole pockets. Note that we solved Eq. (15) using a fast Fourier transform, instead of solving Eq. (24).

Next, we calculate the temperature dependence of the matrix elements of $\hat{\chi}^0(\mathbf{0}, 0)$ using Eq. (15) because it is essential to the following calculations. They are real numbers because $\mathbf{q} = 0$ and $\omega = 0$. $\chi^0_{AA}(\mathbf{0}, 0) = \chi^0_{CC}(\mathbf{0}, 0)$, $\chi^0_{AB}(\mathbf{0}, 0) = \chi^0_{BA}(\mathbf{0}, 0) = \chi^0_{BC}(\mathbf{0}, 0) = \chi^0_{CB}(\mathbf{0}, 0)$, and $\chi^0_{AC}(\mathbf{0}, 0) = \chi^0_{CA}(\mathbf{0}, 0)$ are satisfied owing to space-inversion symmetry and time-reversal symmetry. Figure 11 shows the temperature dependence of the matrix elements of $\hat{\chi}^0(\mathbf{0}, 0)$. The diagonal element $\chi^0_{AA}(\mathbf{0}, 0)$ is almost constant. Furthermore, $\chi^0_{BB}(\mathbf{0}, 0)$ decreases slowly with decreasing temperature. However, the off-diagonal elements $\chi^0_{AB}(\mathbf{0}, 0)$
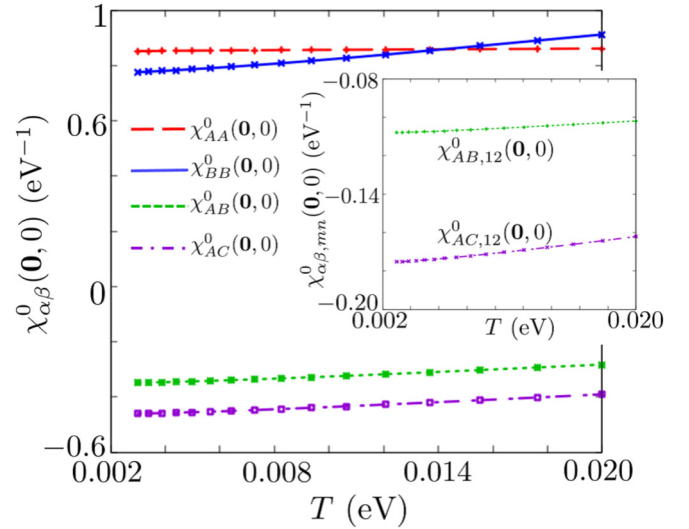

FIG. 11. Temperature dependence of $\chi^0_{\alpha\beta}(\mathbf{0}, 0)$. The red dashed, blue solid, green dotted, and purple chain lines represent $\chi^0_{AA}(\mathbf{0}, 0)$, $\chi^0_{BB}(\mathbf{0}, 0)$, $\chi^0_{AB}(\mathbf{0}, 0)$, and $\chi^0_{AC}(\mathbf{0}, 0)$, respectively. The inset shows the band-dependent spin susceptibilities $\chi^0_{AB,12}(\mathbf{0}, 0)$ and $\chi^0_{AC,12}(\mathbf{0}, 0)$ by the green dotted and purple chain lines, respectively.

and $\chi^0_{AC}(\mathbf{0}, 0)$ are negative and decrease as the temperature decreases. To show what determines the sign of $\chi^0_{AB}(\mathbf{0}, 0)$ and $\chi^0_{AC}(\mathbf{0}, 0)$, we define the band-dependent spin susceptibility as

$$\chi^0_{\alpha\beta,mn}(\mathbf{q}, i\omega_l) = -\frac{T}{N_L} \sum_{\mathbf{k},l'} G^0_{\alpha\beta,m}(\mathbf{k}+\mathbf{q}, i\tilde{\omega}_{l'}+i\omega_l) G^0_{\beta\alpha,n}(\mathbf{k}, i\tilde{\omega}_{l'}),$$
(25)

$$G^0_{\alpha\beta,m,\sigma}(\mathbf{k}, i\tilde{\omega}_l) = d_{\alpha,m,\sigma}(\mathbf{k})d^*_{\beta,m,\sigma}(\mathbf{k})\frac{1}{i\tilde{\omega}_l - \epsilon_{\mathbf{k},m,\sigma}}, \quad (26)$$

where m and n are the band indices. Equation (25) satisfies $\sum_{m,n} \chi^0_{\alpha\beta,mn}(\mathbf{q}, i\omega_l) = \chi^0_{\alpha\beta}(\mathbf{q}, i\omega_l)$, where $\chi^0_{\alpha\beta}(\mathbf{q}, i\omega_l)$ is given by Eq. (15). The inset of Fig. 11 shows the temperature dependence of $\chi^0_{AB,12}(\mathbf{0}, 0)$ and $\chi^0_{AC,12}(\mathbf{0}, 0)$. They are negative. Such terms render the off-diagonal elements of spin susceptibility, $\chi^0_{AB}(\mathbf{0}, 0)$ and $\chi^0_{AC}(\mathbf{0}, 0)$, negative.

B. Knight shift and $1/T_1 T$ in the absence of U

We calculate the Knight shift in the absence of U using Eq. (19). The fragment orbital components of the Knight shift can be given by $K_A = \chi^0_{AA}(\mathbf{0}, 0) + \chi^0_{AB}(\mathbf{0}, 0) + \chi^0_{AC}(\mathbf{0}, 0)$ and $K_B = \chi^0_{BB}(\mathbf{0}, 0) + 2\chi^0_{AB}(\mathbf{0}, 0)$ using the spin susceptibilities in Fig. 11 due to the space-inversion symmetry. Figure 12 shows the Knight shift for the fragment orbitals A(=C) and B in the absence of U. $T = T^* \sim 0.01$ eV is the energy scale where the Fermi surface affects the Knight shift and $1/T_1 T$. $T^* \sim 0.01$ eV is consistent with the energy scale of the Fermi surface. For temperatures higher than T^*, the Knight shift and $1/T_1 T$ are affected by the linear energy dispersion. The Knight shift of the Dirac electron system in the absence of the interaction is given by $K_\alpha \simeq \int_{-\infty}^{\infty} D_\alpha(\omega)(-\frac{df(\omega)}{d\omega})d\omega$ [67]. $f(\omega)$ is the Fermi distribution function for the energy ω. Because $D_\alpha(\omega) \propto \omega$ near the Fermi energy in Fig. 6, K_α is proportional to T for $T \gtrsim T^*$ in Fig. 12. In the two-dimensional Dirac
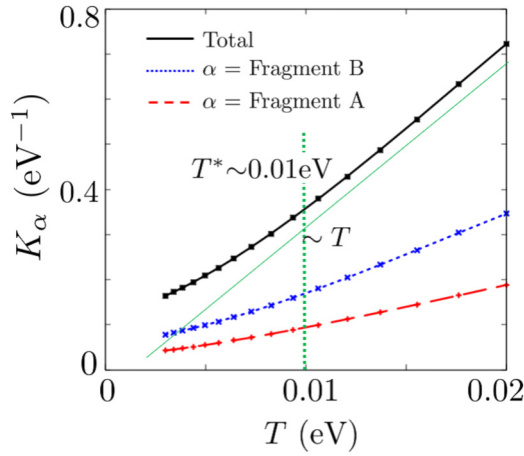
FIG. 12. Temperature dependence of K_α in the absence of U. The red dotted and blue dashed lines show K_A and K_B, respectively. The black solid line shows the total Knight shift $K_{\text{total}} = K_A + K_B + K_C$. The dotted longitudinal line indicates $T = T^* \sim 0.01$ eV. The green thin line which is proportional to T is drawn for the eye guide.

electron system, the Knight shift is proportional to T at low temperature and becomes zero at $T = 0$ because DOS is zero at E_F. However, K_α in this material is not proportional to T for $T \lesssim T^*$ because $D_\alpha(0) \neq 0$ in Fig. 6. This is the effect of the Fermi surface. The magnitude relationship $K_B > K_A$ results from $D_B(\omega) > D_A(\omega)$ near the Fermi energy. Next, we calculate the spin-lattice relaxation rate $1/T_1T$ in the absence of U using Eq. (20). $1/T_1T$ is determined by $\sum_{\mathbf{q}} \text{Im}[\chi^0_{\alpha\alpha}(\mathbf{q}, \omega_0)]$. $\text{Im}[\chi^0_{AA}(\mathbf{q}, \omega_0)]$ and $\text{Im}[\chi^0_{BB}(\mathbf{q}, \omega_0)]$ are shown in Fig. 8. Figure 13 shows the temperature dependence of $1/T_1T$ in the absence of U. $(1/T_1T)_\alpha$ is proportional to T^2 for $T \gtrsim T^*$ in Fig. 12 because the $1/T_1T$ of the Dirac electron system is given by $(1/T_1T)_\alpha \simeq \int_{-\infty}^{\infty} [D_\alpha(\omega)]^2 (-\frac{df(\omega)}{d\omega}) d\omega$ [67]. For $T \lesssim T^*$, $(1/T_1T)_\alpha$ is not proportional to T^2 because of the Fermi surface.
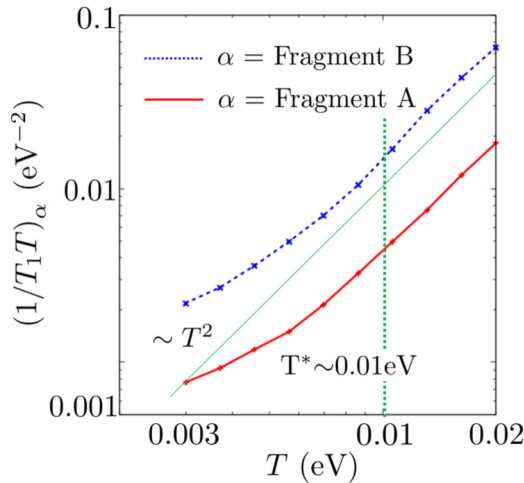

FIG. 13. Temperature dependence of $(1/T_1T)_\alpha$ in the absence of U. The red solid and blue dotted lines show $(1/T_1T)_A$ and $(1/T_1T)_B$, respectively. The dashed longitudinal line indicates $T = T^* \sim 0.01$ eV. The green thin line which is proportional to T^2 is drawn for the eye guide.
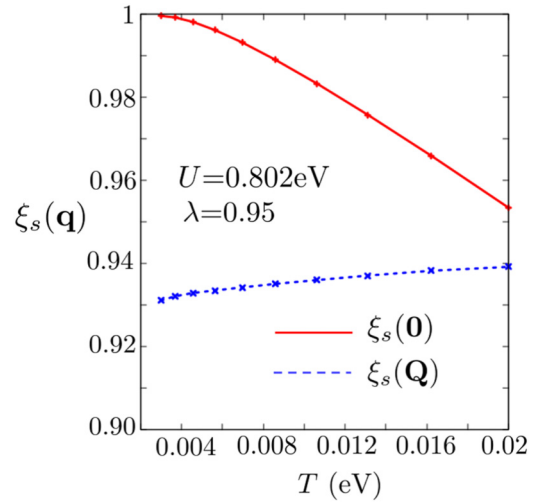

FIG. 14. Temperature dependence of the Stoner factors $\xi_s(\mathbf{0})$ and $\xi_s(\mathbf{Q})$. The red solid and blue dotted lines show $\xi_s(\mathbf{0})$ and $\xi_s(\mathbf{Q})$, respectively.

IV. RESULT IN THE PRESENCE OF U

In this section, we calculate spin fluctuations, the Knight shift, and $1/T_1T$ in the presence of U. It is shown that electron correlation effects are important for explaining the observed temperature dependence of the Knight shift and $1/T_1T$ reported by ^{13}C-NMR experiments [60]. According to Eq. (18), the Stoner factor $\xi_s(\mathbf{q})$ that has a value close to unity gives major contributions to the spin susceptibility and therefore to the Knight shift and $1/T_1T$. Namely, $\xi_s(\mathbf{q} = \mathbf{0}) \approx 1$ becomes predominant for the Knight shift [Eq. (19)], whereas $\xi_s(\mathbf{q} = \mathbf{Q}) \approx 1$ contributes for $1/T_1T$ [Eq. (20)].

A. Spin fluctuations

We calculate the temperature dependence of the Stoner factor $\xi_s(\mathbf{q})$ because $\xi_s(\mathbf{q})$ is an important measurement of spin fluctuations as discussed in Sec. II. Figure 14 shows the temperature dependence of $\xi_s(\mathbf{q})$, where $U = 0.802$ and $\lambda = 0.95$. $\lambda = 0.95$ was obtained in the calculation of the screened Coulomb interaction using RESPACK. In the case of $\lambda = 0.95$, $\xi_s(\mathbf{0})$ is maximum in the momentum space and increases as T decreases. The combination of $\lambda = 0.95$ and $U = 0.802$ yields $\xi_s(\mathbf{0}) = 0.999$ at $T = 0.003$ eV. On the other hand, $\xi_s(\mathbf{Q})$ decreases slowly with decreasing T and is less than $\xi_s(\mathbf{0})$. $\mathbf{Q}$ is the wave number at which $\chi^0_{BB}(\mathbf{q}, 0)$ has the maximum value. $\chi^s_{BB}(\mathbf{q}, 0)$ also has the maximum value at $\mathbf{q} = \mathbf{Q}$. The magnitude relationship $\xi_s(\mathbf{0}) > \xi_s(\mathbf{Q})$ implies that the $\mathbf{q} = \mathbf{0}$ magnetic order is easier to induce than SDW at $\mathbf{q} = \mathbf{Q}$. At a low temperature of $T \lesssim 0.003$eV, it is difficult for $\xi_s(\mathbf{q})$ to converge in the numerical calculation because enormous Matsubara frequencies and wave numbers are required.

We explain why $\xi_s(\mathbf{0})$ increases at low temperature. In fact, $\xi_s(\mathbf{q})$ is not directly determined by the DOS because the maximum eigenvalue of $\hat{U}\hat{\chi}^0(\mathbf{q}, 0)$ contains the products of the $\chi^0_{\alpha\beta}(\mathbf{q}, 0)$. It means that the electron correlation effect is important. We calculate the first- and second-order perturbation terms in in Figs. 4(a) and 4(b). In this study, Figs. 4(a)
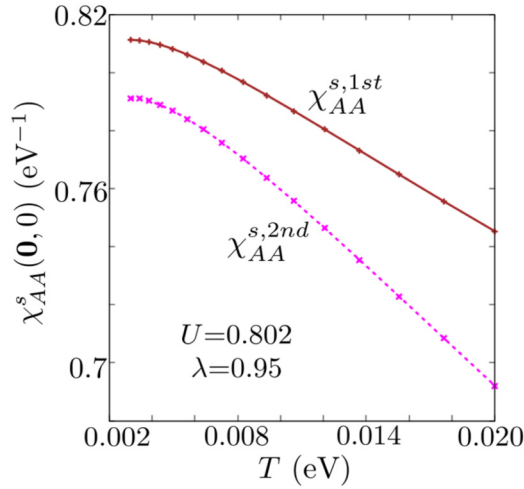
FIG. 15. First- and second-order perturbation terms of $\chi_{AA}^s(\mathbf{0}, 0)$ shown by the brown solid and magenta dotted lines, respectively. The horizontal axis represents the temperature.

and 4(b) are equivalent. Their matrix elements $\chi_{\alpha\beta}^{s,1st}(\mathbf{q}, i\omega_l)$ and $\chi_{\alpha\beta}^{s,2nd}(\mathbf{q}, i\omega_l)$ are written as

$$\chi_{\alpha\beta}^{s,1st}(\mathbf{q}, i\omega_l) = \sum_{\gamma} \chi_{\alpha\gamma}^0(\mathbf{q}, i\omega_l) U_{\gamma\gamma} \chi_{\gamma\beta}^0(\mathbf{q}, i\omega_l), \quad (27)$$

$$\chi_{\alpha\beta}^{s,2nd}(\mathbf{q}, i\omega_l) = \sum_{\gamma,\gamma'} \chi_{\alpha\gamma}^0(\mathbf{q}, i\omega_l) U_{\gamma\gamma} \chi_{\gamma\gamma'}^0(\mathbf{q}, i\omega_l)$$

$$\times U_{\gamma'\gamma'} \chi_{\gamma'\beta}^0(\mathbf{q}, i\omega_l). \quad (28)$$

They are the first- and second-order perturbation terms in RPA and correspond to the second and third terms in Figs. 4(a) and 4(b), respectively. Figure 15 shows the temperature dependence of $\chi_{AA}^{s,1st}(\mathbf{0}, 0)$ and $\chi_{AA}^{s,2nd}(\mathbf{0}, 0)$. They increase as T decreases. Note that the zero-order perturbation term is identical to the red dashed line in Fig. 11. Since the off-diagonal elements of $\hat{\chi}^0(\mathbf{0}, 0)$ are negative and decrease as T decreases in Fig. 11, their absolute squares increase as T decreases. Thus, terms such as $\chi_{AB}^0(\mathbf{0}, 0) U_{BB} \chi_{BA}^0(\mathbf{0}, 0)$ in Eq. (27) and $\chi_{AC}^0(\mathbf{0}, 0) U_{CC} \chi_{CC}^0(\mathbf{0}, 0) U_{CC} \chi_{CA}^0(\mathbf{0}, 0)$ in Eq. (28) increase $\chi_{AA}^{s,1st}(\mathbf{0}, 0)$ and $\chi_{AA}^{s,2nd}(\mathbf{0}, 0)$ at low temperature. The other higher-order perturbation terms behave similarly. Therefore, $\xi_s(\mathbf{0})$ increases as T decreases.

Fragment orbitals A and C are sensitive to $\xi_s(\mathbf{0})$. On the other hand, fragment orbital B is insensitive to $\xi_s(\mathbf{0})$ but sensitive to $\xi_s(\mathbf{Q})$. We calculate the matrix elements of $\hat{\chi}^s(\mathbf{0}, 0)$ and $\hat{\chi}^s(\mathbf{Q}, 0)$ to exhibit this phenomenon using Eqs. (15) and (17). Figure 16(a) shows the temperature dependence of $\chi_{AA}^s(\mathbf{0}, 0)$, $\chi_{BB}^s(\mathbf{0}, 0)$, $\chi_{AB}^s(\mathbf{0}, 0)$, and $\chi_{AC}^s(\mathbf{0}, 0)$. They are real numbers because $\mathbf{q} = 0$ and $\omega = 0$. $\chi_{AA}^s(\mathbf{0}, 0) = \chi_{CC}^s(\mathbf{0}, 0)$, $\chi_{AB}^s(\mathbf{0}, 0) = \chi_{BA}^s(\mathbf{0}, 0) = \chi_{BC}^s(\mathbf{0}, 0) = \chi_{CB}^s(\mathbf{0}, 0)$, and $\chi_{AC}^s(\mathbf{0}, 0) = \chi_{CA}^s(\mathbf{0}, 0)$ are satisfied because of space-inversion symmetry and time-reversal symmetry. The inset shows an enlarged view of the region around $\chi_{BB}^s(\mathbf{0}, 0)$ and $\chi_{AB}^s(\mathbf{0}, 0)$. $\chi_{BB}^s(\mathbf{0}, 0)$ and $\chi_{AB}^s(\mathbf{0}, 0)$ are difficult to increase at low temperature, whereas $\chi_{AA}^s(\mathbf{0}, 0)$ sharply increases. Moreover, $\chi_{AC}^s(\mathbf{0}, 0)$ is negative and sharply decreases as T decreases. $\xi_s(\mathbf{0})$ easily affects fragment orbitals A and C but not fragment orbital B. The situation of $\chi_{AC}^s(\mathbf{0}, 0) < 0$
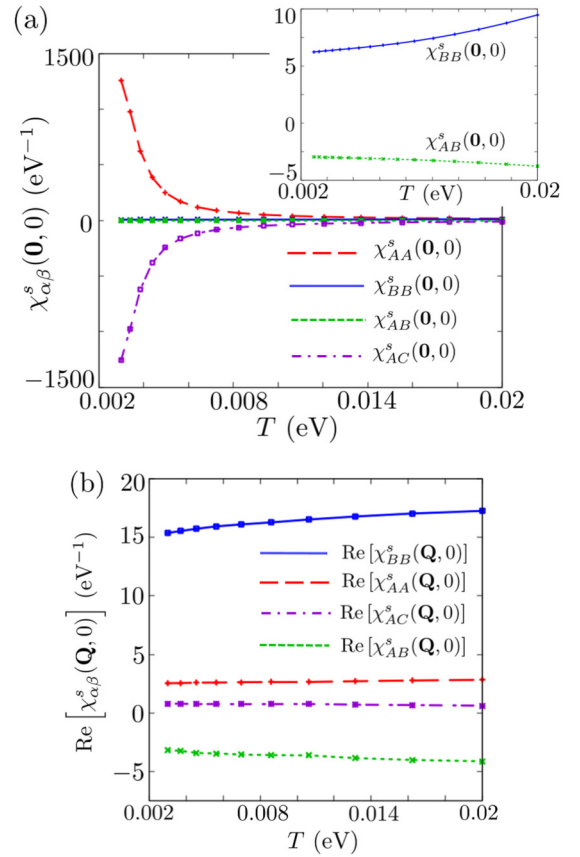

FIG. 16. (a) Temperature dependence of $\chi_{AA}^s(\mathbf{0}, 0)$, $\chi_{BB}^s(\mathbf{0}, 0)$, $\chi_{AB}^s(\mathbf{0}, 0)$, and $\chi_{AC}^s(\mathbf{0}, 0)$ shown by the red dashed, blue solid, green dotted, and purple chain lines, respectively. The inset shows an enlarged view of the region around $\chi_{BB}^s(\mathbf{0}, 0)$ and $\chi_{AB}^s(\mathbf{0}, 0)$. (b) Temperature dependence of Re[$\chi_{AA}^s(\mathbf{Q}, 0)$], Re[$\chi_{BB}^s(\mathbf{Q}, 0)$], Re[$\chi_{AB}^s(\mathbf{Q}, 0)$], and Re[$\chi_{AC}^s(\mathbf{Q}, 0)$]. The combination of matrix elements and lines is the same as in (a).

in Fig. 16(a) implies intramolecular antiferromagnetic fluctuations. The negative off-diagonal elements of the spin susceptibility are due to the characteristic wave function of the Dirac nodal line system.

Figure 16(b) shows the temperature dependence of Re[$\chi_{AA}^s(\mathbf{Q}, 0)$], Re[$\chi_{BB}^s(\mathbf{Q}, 0)$], Re[$\chi_{AB}^s(\mathbf{Q}, 0)$], and Re[$\chi_{AC}^s(\mathbf{Q}, 0)$]. Re[$\hat{\chi}^s(\mathbf{Q}, 0)$] reflects $\xi_s(\mathbf{Q})$ and slowly varies with temperature. At $\mathbf{q} = \mathbf{Q}$, Re[$\chi_{BB}^s(\mathbf{Q}, 0)$] is the largest of all matrix elements and increases with temperature. Fragment orbital B is sensitive to $\xi_s(\mathbf{Q})$. Because Re[$\chi_{AB}^s(\mathbf{Q}, 0)$] < 0 and Re[$\chi_{AC}^s(\mathbf{Q}, 0)$] > 0, the spins of the fragment orbitals B and A(C) within a molecule are inversely correlated.

Figure 17 schematically illustrates the spin polarization pictures that we obtained from the calculated results in Fig. 16 for the paramagnetic regime. Figure 17(a) corresponds to the case in Fig. 16(a), where we find intramolecular antiferromagnetic spin fluctuations, which are commensurate($\mathbf{q} = \mathbf{0}$) between molecules. The solid arrows in Fig. 17(a) represents a tendency where an infinitesimally small downward local magnetic field at the orbital C(A) induces an upward spin polarization at the orbital A(C) by the linear response relation $M_{A(C)} = \chi_{AC(CA)}^s H_{C(A)}$, respectively [$M$ is the magnetization and H is the infinitesimal magnetic field]. Figure 17(b), which
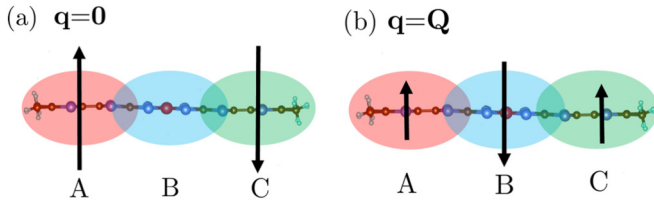
FIG. 17. Schematic illustrations of spin polarization. (a) Intramolecular antiferromagnetic spin fluctuations linked to the $\mathbf{q} = \mathbf{0}$ response shown in Fig. 16(a). (b) Spin correlations within a molecule given by the $\mathbf{q} = \mathbf{Q}$ response in Fig. 16(b).

is derived from Fig. 16(b), stand for the spin fluctuations within a molecule that are incommensurate ($\mathbf{q} = \mathbf{Q}$) between molecules. In this case, the spins at the orbitals A($=$C) and B tend to be inversely correlated within a molecule.

Next, we show the diagonal elements of the spin susceptibilities $\chi_{\alpha\alpha}^s(\mathbf{q}, \omega)$ at $T = 0.003$ eV. Figures 18(a), 18(b), 18(c), and 18(d) show $\chi_{AA}^s(\mathbf{q}, 0)$, $\chi_{BB}^s(\mathbf{q}, 0)$, Im$[\chi_{AA}^s(\mathbf{q}, \omega_0)]$, and Im$[\chi_{BB}^s(\mathbf{q}, \omega_0)]$ in the q_b-q_c plane, respectively. $\chi_{\alpha\alpha}^s(\mathbf{q}, 0)$ is a real number. We fix $q_a = 0$ in Figs. 18(a) and 18(c) and $q_a = 0.2\pi$ in Figs. 18(b) and 18(d). Furthermore, ω_0 is equal to 0.001 eV. Re$[\chi_{AA}^s(\mathbf{q}, 0)]$ and Im$[\chi_{AA}^s(\mathbf{q}, \omega_0)]$ have very large values at $\mathbf{q} = \mathbf{0}$ because $\xi_s(\mathbf{0}) = 0.999$. However, the BB component is difficult to be affected by $\xi_s(\mathbf{0})$ but easily affected by $\xi_s(\mathbf{Q})$. $\mathbf{Q}$ is the wave number at which $\chi_{BB}^0(\mathbf{q}, 0)$ and $\chi_{BB}^s(\mathbf{q}, 0)$ have the maximum values. $\chi_{AA}^s(\mathbf{0}, 0)$ and Im$[\chi_{AA}^s(\mathbf{0}, \omega_0)]$ are much larger than $\chi_{BB}^s(\mathbf{Q}, 0)$ and Im$[\chi_{BB}^s(\mathbf{Q}, \omega_0)]$ because $\xi_s(\mathbf{0}) > \xi_s(\mathbf{Q})$ and the spin susceptibility obtained using RPA is determined by $1/(1 - \xi_s(\mathbf{q}))$. $\chi_{AA}^s(\mathbf{0}, 0)$ and Im$[\chi_{AA}^s(\mathbf{0}, \omega_0)]$ in Figs. 18(a) and 18(c) decrease with temperature. On the other hand, $\chi_{BB}^s(\mathbf{Q}, 0)$ and Im$[\chi_{BB}^s(\mathbf{Q}, \omega_0)]$ in Figs. 18(b) and 18(d) slowly increase and
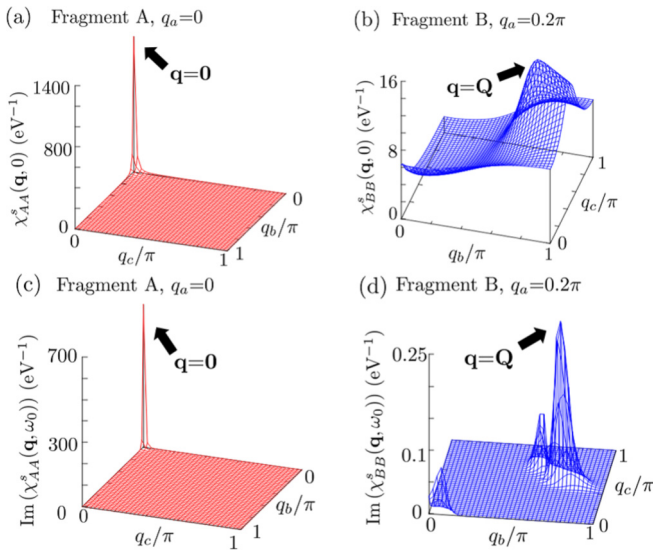

FIG. 18. The momentum dependencies of the diagonal elements of the spin susceptibility in the presence of U (a) $\chi_{AA}^s(\mathbf{q}, 0)$ in the q_b–q_c plane, where $q_a = 0$. (b) $\chi_{BB}^s(\mathbf{q}, 0)$ in the q_b–q_c plane, where $q_a = 0.2\pi$. (c) Im$[\chi_{AA}^s(\mathbf{q}, \omega_0)]$ in the q_b–q_c plane, where $q_a = 0$. (d) Im$[\chi_{BB}^s(\mathbf{q}, \omega_0)]$ in the q_b–q_c plane, where $q_a = 0.2\pi$. The temperature $T = 0.003$ eV.
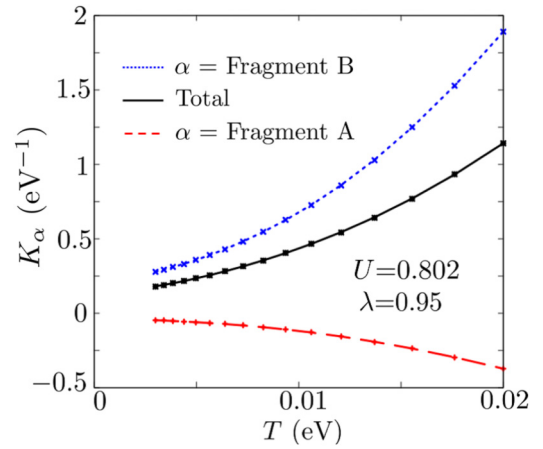

FIG. 19. Temperature dependence of the Knight shift K_α for $U = 0.802$ and $\lambda = 0.95$. The red dashed and blue dotted lines show K_A and K_B, respectively. The black solid line shows the total Knight shift $K_{\text{tot}} = K_A + K_B + K_C$.

the peaks become broad with temperature. These behavior result from the temperature dependence of $\xi_s(\mathbf{q})$ in Fig. 14.

B. Knight shift and $1/T_1T$ in the presence of U

In this subsection, we solve Eqs. (19) and (20) to investigate the effects of the fluctuations on the Knight shift and $1/T_1T$.

Figure 19 shows the temperature dependence of the Knight shift, where $U = 0.802$ and $\lambda = 0.95$. K_B in the presence of U is larger than that in the absence of U. However, K_A and K_C in the presence of U are smaller than those in the absence of U. In the case of $U = 0.802$ and $\lambda = 0.95$, K_A and K_C are negative, while K_B and $K_{\text{tot}}(= K_A + K_B + K_C)$ are positive. Similar behavior was previously observed in the organic conductor α-(BEDT-TTF)$_2$I$_3$ [30].

K_A and K_C do not increase at low temperature, although the Stoner factor $\xi_s(\mathbf{0})$ is almost 1 at $T = 0.003$ eV. The behavior of the Knight shift is understood by considering the off-diagonal elements of $\hat{\chi}^s(\mathbf{0}, 0)$. Because $\chi_{AA}^s(\mathbf{0}, 0)$ and $\chi_{AC}^s(\mathbf{0}, 0)$ have opposite signs in Fig. 16(a), their cancellation prevents the increase of the Knight shift in Eq. (19). In other words, the $\mathbf{q} = \mathbf{0}$ spin fluctuations are not observed in the Knight shift because of the intramolecular antiferromagnetic fluctuations.

Next, we solve Eq. (20). The spin-lattice relaxation rate, $1/T_1T$, is determined by $\sum_{\mathbf{q}} \text{Im}[\chi_{\alpha\alpha}^s(\mathbf{q}, \omega_0)]$. Im$[\chi_{AA}^s(\mathbf{q}, \omega_0)]$ and Im$[\chi_{BB}^s(\mathbf{q}, \omega_0)]$ are shown in Fig. 18. Figure 20 shows the temperature dependence of $1/T_1T$, where $\lambda = 0.95$ and $U = 0.802$. At high temperature, $1/T_1T$ values for all orbitals decrease with decreasing T. However, at low temperature, the $(1/T_1T)_A$ starts to increase because orbital A is easily affected by $\xi_s(\mathbf{0})$. The behavior of $(1/T_1T)_C$ is identical to that of $(1/T_1T)_A$ because of space-inversion symmetry. Although $(1/T_1T)_B$ is difficult to be affected by $\xi_s(\mathbf{0})$ in Fig. 20, $\xi_s(\mathbf{0}) \rightarrow 1$ makes $(1/T_1T)_B \rightarrow \infty$. This is because $\xi_s(\mathbf{0}) \rightarrow 1$ makes $1/[1 - \xi_s(\mathbf{0})] \rightarrow \infty$ and RPA imposes the factor $1/[1 - \xi_s(\mathbf{0})]$ on the spin susceptibility [Eq. (18)]. For $T \gtrsim 0.005$ eV, $(1/T_1T)_B$ is more dominant than $(1/T_1T)_A$ and
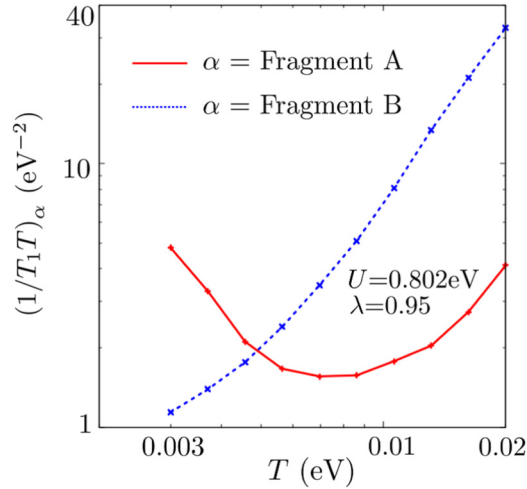
FIG. 20. Temperature dependence of $(1/T_1T)_\alpha$ for $U = 0.802$ and $\lambda = 0.95$. The red solid and blue dotted lines show $(1/T_1T)_A$ and $(1/T_1T)_B$, respectively.

FIG. 21. Correspondence table between the fragment orbitals, shape of the Fermi surface, momenta at which the noninteracting spin susceptibilities have peaks, Stoner factors, and $1/T_1T$.

V. CONCLUSION

In this study, we found that multiple fragment orbitals play important roles in the magnetic properties of [Ni(dmdt)$_2$]. On orbitals A and C, which are unevenly distributed toward one side of a molecule, the $\mathbf{q} = \mathbf{0}$ spin fluctuations are enhanced, whereas the incommensurate spin fluctuations are enhanced on orbital B, which is centered on the Ni atom. Because of the $\mathbf{q} = \mathbf{0}$ spin fluctuations, the A and C components of $1/T_1T$ start to increase as T decreases at low temperature. However, the $\mathbf{q} = \mathbf{0}$ spin fluctuations do not affect the Knight shift because they are incommensurate antiferromagnetic fluctuations. The reason why the $\mathbf{q} = \mathbf{0}$ spin fluctuations are enhanced is understood from the perturbation process and the off-diagonal elements of the noninteracting spin susceptibility. The incommensurate spin fluctuations dominantly contribute to the B component of $1/T_1T$ at high temperature. These fragment-orbital-dependent quantities result from the presence of ZR. If no ZR exists in the Brillouin zone, the BB components of the spin susceptibilities do not have the maximum value at the incommensurate wave number because the spectral weight of fragment orbital B at E_F may be similar to those of A and C. Because ZR biases $\rho_B(\mathbf{k}, 0)$ in Eq. (23) to a part of the Fermi surface, the BB component of the spin susceptibility has a maximum value at the incommensurate wave number $\mathbf{q} = \mathbf{Q}$. Thus, the wave number dependence of the spin susceptibilities is different between the BB component and AA(CC) component. ZR is a characteristic of materials with a Dirac nodal line system described by an n-band model($n \geqslant 3$). Thus, it is expected that the fragment-orbital-dependent properties due to ZR will be found in other Dirac nodal line systems. Moreover, it is predicted that transition-metal substitution in the Ni(dmdt)$_2$ molecule controls spin fluctuations because it changes λ and U. In the two-dimensional Dirac electron system under the charge-neutral condition, the spin fluctuations are weak because the Fermi surface is identical to the Dirac points. On the other hand, the spin fluctuations are enhanced in [Ni(dmdt)$_2$] by the Fermi surface. The Fermi surface arises from transfer integrals in the nodal line direction. This is the three dimensionality of this material.

In the ^{13}C-NMR experiment, $1/T_1T$ has a peak at $T \sim$ 30 K. The experiment was performed for a sample in which C atoms were replaced with ^{13}C. Figure 2(b) shows a Ni(dmdt)$_2$

$(1/T_1T)_C$ because $\xi_s(\mathbf{Q})$ slowly increases with T and orbital B is easier to be affected by $\xi_s(\mathbf{Q})$. $\mathbf{Q}$ is the wave number at which $\chi_{BB}^0(\mathbf{q}, 0)$ and $\chi_{BB}^s(\mathbf{q}, 0)$ have the maximum values.

In the case of a small λ, such as $\lambda = 0.79$, $\xi_s(\mathbf{Q})$ is larger than $\xi_s(\mathbf{0})$, and SDW can be induced. However, the incommensurate spin fluctuations in this material are suppressed at low temperature in Fig. 14. Similar behavior occurs in the case of a small λ. If U is sufficiently large, $\xi_s(\mathbf{Q})$ reaches 1 at low temperature. However, the magnetic transition to the SDW phase would have already been induced at a high temperature. Thus, it is difficult to explain the upturn of the $1/T_1T$ curve near 30 K, which is observed in the ^{13}C-NMR experiment, by the incommensurate spin fluctuations. We calculate λ using the RESPACK program. Because $\lambda = 0.79$ is obtained as the ratio of diagonal elements with the unscreened on-site Coulomb interaction while $\lambda = 0.95$ is obtained as that with the screened on-site Coulomb interaction, we consider that $\lambda = 0.95$ is the more realistic ratio.

In this subsection, we showed that the Knight shift does not increase at low temperature because of the intramolecular antiferromagnetic fluctuations. We also showed that the $(1/T_1T)_A$ and $(1/T_1T)_C$ start to increase at low temperature because of the behavior of $\xi_s(\mathbf{0})$. They are dominant in $T \lesssim 0.005$ eV, whereas $(1/T_1T)_B$ is dominant in $T \gtrsim$ 0.005 eV because of the temperature dependence of $\xi_s(\mathbf{Q})$ and fragment-orbital-dependence of spin susceptibilities. Figure 21 summarizes the fragment-orbital dependence of the Fermi surface, noninteracting spin susceptibilities, Stoner factors, and $1/T_1T$. Figure 21 shows the important factors for orbitals A and B. $\xi_s(\mathbf{0})$ is the main contributor to orbital A and causes the upturn of the $(1/T_1T)_A$ curve at low temperature. However, the contribution of $\xi_s(\mathbf{0})$ to orbital B is small. Orbital B is sensitive to $\xi_s(\mathbf{Q})$, which dominantly contributes to $(1/T_1T)_B$ at high temperature, but does not contribute to orbital A as much. These fragment-orbital-dependent magnetic properties are caused by the presence of ZR because ZR biases $\rho_B(\mathbf{k}, 0)$ in Eq. (23) to a part of the Fermi surface.

molecule, and the red dashed circles surround ^{13}C atoms. Therefore, orbitals A and C mainly contribute to the physical quantities observed in the ^{13}C-NMR experiment. Thus, our calculation of $1/T_1T$ is almost consistent with the experiment. Furthermore, we expect that the B component of $1/T_1T$ can be observed by experiments using a sample in which ^{12}C atoms near the Ni atom are substituted by ^{13}C. On the other hand, the A and C components of the Knight shift obtained in our calculation are negative, but the Knight shift observed in the ^{13}C-NMR experiment is positive. Therefore, we consider the following possible electronic states at $T \lesssim 30$ K. The first is the $\mathbf{q} = \mathbf{0}$ magnetic ordered state, which is the intramolecular antiferromagnetism is realized at $T \lesssim 30$ K. In this case, it is considered that the Knight shift observed in the experiment is attributed to the sum of K_A and K_B, which is positive. In the second possible electronic state, U is not so large that K_A

is negative. In this case, it is considered that another ordered state is induced at $T \lesssim 30$ K and that the $1/T_1T$ curve is upturned by the fluctuations corresponding to the order. Examples of such orders are bond order and topological order.

[1] T. Ando, T. Nakanishi, and R. Saito, J. Phys. Soc. Jpn. **67**, 2857 (1998).

[2] V. P. Gusynin and S. G. Sharapov, Phys. Rev. B **73**, 245411 (2006).

[3] S. Murakami, N. Nagaosa, and S.-C. Zhang, Phys. Rev. Lett. **93**, 156804 (2004).

[4] D. Hsieh, D. Qian, L. Wray, Y. Xia, Y. S. Hor, R. J. Cava, and M. Z. Hasan, Nature (London) **452**, 970 (2008).

[5] H. Fukuyama and R. Kubo, J. Phys. Soc. Jpn. **28**, 570 (1970).

[6] H. Fukuyama, J. Phys. Soc. Jpn. **76**, 043711 (2007).

[7] A. A. Abrikosov and S. D. Beneslavskii, Zh. Eksp. Teor. Fiz. **59**, 1280 (1971) [Sov. Phys. JETP **32**, 699 (1971)].

[8] J. González, F. Guinea, and M. A. H. Vozmediano, Nucl. Phys. B **424**, 595 (1994).

[9] J. González, F. Guinea, and M. A. H. Vozmediano, Phys. Rev. B **59**, R2474 (1999).

[10] V. N. Kotov, B. Uchoa, V. M. Pereira, F. Guinea, and A. H. Castro Neto, Rev. Mod. Phys. **84**, 1067 (2012).

[11] T. O. Wehling, A. M. Black-Schaffer, and A. V. Balatsky, Adv. Phys. **63**, 1 (2014).

[12] W. Witczak-Krempa, G. Chen, Y. B. Kim, and L. Balents, Annu. Rev. Condens. Matter Phys. **5**, 57 (2014).

[13] K. Kajita, T. Ojiro, H. Fujii, Y. Nishio, H. Kobayashi, A. Kobayashi, and R. Kato, J. Phys. Soc. Jpn. **61**, 23 (1992).

[14] N. Tajima, M. Tamura, Y. Nishio, K. Kajita, and Y. Iye, J. Phys. Soc. Jpn. **69**, 543 (2000).

[15] A. Kobayashi, S. Katayama, K. Noguchi, and Y. Suzumura, J. Phys. Soc. Jpn. **73**, 3135 (2004).

[16] S. Katayama, A. Kobayashi, and Y. Suzumura, J. Phys. Soc. Jpn. **75**, 054705 (2006).

[17] A. Kobayashi, S. Katayama, Y. Suzumura, and H. Fukuyama, J. Phys. Soc. Jpn. **76**, 034711 (2007).

[18] M. O. Goerbig, J. N. Fuchs, G. Montambaux, and F. Piéchon, Phys. Rev. B **78**, 045415 (2008).

[19] K. Kajita, Y. Nishio, N. Tajima, Y. Suzumura, and A. Kobayashi, J. Phys. Soc. Jpn. **83**, 072002 (2014).

[20] H. Seo, J. Phys. Soc. Jpn. **69**, 805 (2000).

[21] T. Takahashi, Synth. Met. **133-134**, 261 (2003).

[22] T. Kakiuchi, Y. Wakabayashi, H. Sawa, T. Takahashi, and T. Nakamura, J. Phys. Soc. Jpn. **76**, 113702 (2007).

[23] K. Ishikawa, M. Hirata, D. Liu, K. Miyagawa, M. Tamura, and K. Kanoda, Phys. Rev. B **94**, 085154 (2016).

[24] Y. Tanaka and M. Ogata, J. Phys. Soc. Jpn. **85**, 104706 (2016).

[25] R. Beyer, A. Dengl, T. Peterseim, S. Wackerow, T. Ivek, A. V. Pronin, D. Schweitzer, and M. Dressel, Phys. Rev. B **93**, 195116 (2016).

[26] D. Liu, K. Ishikawa, R. Takehara, K. Miyagawa, M. Tamura, and K. Kanoda, Phys. Rev. Lett. **116**, 226401 (2016).

[27] D. Ohki, Y. Omori, and A. Kobayashi, Phys. Rev. B **100**, 075206 (2019).

[28] M. Hirata, K. Ishikawa, K. Miyagawa, M. Tamura, C. Berthier, D. Basko, A. Kobayashi, G. Matsuno, and K. Kanoda, Nat. Commun. **7**, 12666 (2016).

[29] M. Hirata, K. Ishikawa, G. Matsuno, A. Kobayashi, K. Miyagawa, M. Tamura, C. Berthier, and K. Kanoda, Science **358**, 1403 (2017).

[30] A. Kobayashi and Y. Suzumura, J. Phys. Soc. Jpn. **82**, 054715 (2013).

[31] D. Ohki, M. Hirata, T. Tani, K. Kanoda, and A. Kobayashi, Phys. Rev. Res. **2**, 033479 (2020).

[32] M. Hirata, A. Kobayashi, C. Berthier, and K. Kanoda, Rep. Prog. Phys. **84**, 036502 (2021).

[33] A. A. Burkov, M. D. Hook, and L. Balents, Phys. Rev. B **84**, 235126 (2011).

[34] C. K. Chiu and A. P. Schnyder, Phys. Rev. B **90**, 205136 (2014).

[35] C. Fang, Y. Chen, H. Y. Kee, and L. Fu, Phys. Rev. B **92**, 081201(R) (2015).

[36] Z. Gao, M. Hua, H. Zhang, and X. Zhang, Phys. Rev. B **93**, 205109 (2016).

[37] P. R. Wallace, Phys. Rev. **71**, 622 (1947).

[38] H. Weng, C. Fang, Z. Fang, B. A. Bernevig, and X. Dai, Phys. Rev. X **5**, 011029 (2015).

[39] Y. Kim, B. J. Wieder, C. L. Kane, and A. M. Rappe, Phys. Rev. Lett. **115**, 036806 (2015).

[40] R. Yu, H. Weng, Z. Fang, X. Dai, and X. Hu, Phys. Rev. Lett. **115**, 036807 (2015).

[41] J. M. Carter, V. V. Shankar, M. A. Zeb, and H. Y. Kee, Phys. Rev. B **85**, 115105 (2012).

[42] A. Yamakage, Y. Yamakawa, Y. Tanaka, and Y. Okamoto, J. Phys. Soc. Jpn. **85**, 013708 (2016).

[43] R. Kato, H. Cui, T. Tsumuraya, T. Miyazaki, and Y. Suzumura, J. Am. Chem. Soc. **139**, 1770 (2017).

[44] R. Kato and Y. Suzumura, J. Phys. Soc. Jpn. **86**, 064705 (2017).

[45] Y. Suzumura, J. Phys. Soc. Jpn. **86**, 124710 (2017).

[46] Y. Suzumura and R. Kato, Jpn. J. Appl. Phys. **56**, 05FB02 (2017).

[47] Y. Suzumura, H. Cui, and R. Kato, J. Phys. Soc. Jpn. **87**, 084702 (2018).

[48] Y. Suzumura and A. Yamakage, J. Phys. Soc. Jpn. **87**, 093704 (2018).

[49] T. Tsumuraya, R. Kato, and Y. Suzumura, J. Phys. Soc. Jpn. **87**, 113701 (2018).

[50] Y. Suzumura, T. Tsumuraya, R. Kato, H. Matsuura, and M. Ogata, J. Phys. Soc. Jpn. **88**, 124704 (2019).

[51] B. Zhou, S. Ishibashi, T. Ishii, T. Sekine, R. Takehara, K. Miyagawa, K. Kanoda, E. Nishibori, and A. Kobayashi, Chem. Commun. **55**, 3327 (2019).

[52] R. Kato and Y. Suzumura, J. Phys. Soc. Jpn. **89**, 044713 (2020).

[53] T. Kawamura, D. Ohki, B. Zhou, A. Kobayashi, and A. Kobayashi, J. Phys. Soc. Jpn. **89**, 074704 (2020).

[54] T. Kawamura, B. Zhou, A. Kobayashi, and A. Kobayashi, J. Phys. Soc. Jpn. **90**, 064710 (2021).

[55] A. Kobayashi, B. Zhou, R. Takagi, K. Miyagawa, S. Ishibashi, A. Kobayashi, T. Kawamura, E. Nishibori, and K. Kanoda, Bull. Chem. Soc. Jpn. **94**, 2540 (2021).

[56] J. W. Rhim and Y. B. Kim, Phys. Rev. B **92**, 045126 (2015).

[57] A. K. Mitchell and L. Fritz, Phys. Rev. B **92**, 121109(R) (2015).

[58] S. T. Ramamurthy and T. L. Hughes, Phys. Rev. B **95**, 075138 (2017).

[59] N. H. Shon and T. Ando, J. Phys. Soc. Jpn. **67**, 2421 (1998).

[60] T. Sekine, T. Hatamura, K. Sunami, K. Miyagawa, and K. Kanoda (Private Communication).

[61] H. Seo, S. Ishibashi, Y. Okano, H. Kobayashi, A. Kobayashi, H. Fukuyama, and K. Terakura, J. Phys. Soc. Jpn. **77**, 023714 (2008).

[62] H. Seo, S. Ishibashi, Y. Otsuka, H. Fukuyama, and K. Terakura, J. Phys. Soc. Jpn. **82**, 054711 (2013).

[63] M. Tsuchiizu, Y. Omori, Y. Suzumura, M.-L. Bonnet, and V. Robert, J. Chem. Phys. **136**, 044519 (2012).

[64] M. Tsuchiizu, Y. Omori, Y. Suzumura, M-L. Bonnet, V. Robert, S. Ishibashi, and H. Seo, J. Phys. Soc. Jpn. **80**, 013703 (2011).

[65] K. Nakamura, Y. Yoshimoto, Y. Nomura, T. Tadano, M. Kawamura, T. Kosugi, K. Yoshimi, T. Misawa, and Y. Motoyama, Comput. Phys. Commun. **261**, 107781 (2021).

[66] P. Giannozzi, Jr., O. Andreussi, T. Brumme, O. Bunau, M. Buongiorno Nardelli, M. Calandra, R. Car, C. Cavazzoni, D. Ceresoli, M. Cococcioni, N. Colonna, I. Carnimeo, A. Dal Corso, S. de Gironcoli, P. Delugas, R. A. DiStasio, Jr., A. Ferretti, A. Floris, G. Fratesi, G. Fugallo, R. Gebauer, U. Gerstmann, F. Giustino *et al.* J. Phys.: Condens. Matter **29**, 465901 (2017).

[67] S. Katayama, A. Kobayashi, and Y. Suzumura, Eur. Phys. J. B **67**, 139 (2009).